

Gas emissions in Planck cold dust clumps
—A Survey of the J=1-0 Transitions of ^{12}CO , ^{13}CO , and C^{18}O

Yuefang Wu¹, Tie Liu¹, Fanyi Meng², Di Li^{3,4,5}, Sheng-Li Qin⁶, Bing-Gang Ju^{7,8}

Received _____; accepted _____

Accepted to ApJ

¹Department of Astronomy, Peking University, 100871, Beijing, China; ywu@pku.edu.cn

²Yuan Pei school, Peking University, 100871, Beijing China

³ National Astronomical Observatories, CAS, Chaoyang Dist., Datun Rd, A20, Beijing 100012, China

⁴Space Science Institute, Boulder, CO, USA

⁵Jet Propulsion Laboratory, California Institute of Technology, Pasadena, CA

⁶I. Physikalisches Institut, Universität zu Köln, Zùlpicher Str. 77, 50937

⁷Purple Mountain Observatory, Qinghai Station, 817000, Delingha, China

⁸Key Laboratory for Radio Astronomy, CAS

ABSTRACT

A survey toward 674 Planck cold clumps of the Early Cold Core Catalogue (ECC) in the J=1-0 transitions of ^{12}CO , ^{13}CO and C^{18}O has been carried out using the PMO 13.7 m telescope. 673 clumps were detected with the ^{12}CO and ^{13}CO , and 68% of the samples have C^{18}O emission. Additional velocity components were also identified. A close consistency of the three line peak velocities was revealed for the first time. Kinematic distances are given out for all the velocity components and half of the clumps are located within 0.5 and 1.5 kpc. Excitation temperatures range from 4 to 27 K, slightly larger than those of T_d . Line width analysis shows that the majority of ECC clumps are low mass clumps. Column densities N_{H_2} span from 10^{20} to $4.5 \times 10^{22} \text{ cm}^{-2}$ with an average value of $(4.4 \pm 3.6) \times 10^{21} \text{ cm}^{-2}$. N_{H_2} cumulative fraction distribution deviates from the lognormal distribution, which is attributed to optical depth. The average abundance ratio of the ^{13}CO to C^{18}O in these clumps is 7.0 ± 3.8 , higher than the terrestrial value. Dust and gas are well coupled in 95% of the clumps. Blue profile, red profile and line asymmetry in total was found in less than 10% of the clumps, generally indicating star formation is not developed yet. Ten clumps were mapped. Twelve velocity components and 22 cores were obtained. Their morphologies include extended diffuse, dense isolated, cometary and filament, of which the last is the majority. 20 cores are starless. Only 7 cores seem to be in gravitationally bound state. Planck cold clumps are the most quiescent among the samples of weak-red IRAS, infrared dark clouds, UC HII region candidates, EGOs and methanol maser sources, suggesting that Planck cold clumps have expanded the horizon of cold Astronomy.

Subject headings: ISM: clouds - ISM: structure-ISM: kinematics and dynamics - Stars: formation - Stars: protostars

1. Introduction

Large samples significantly improve our understanding of star formation. At the beginning of star formation studies in the early 70s, the Palomar Sky Survey (PSS) plates provided astronomers optical selected nebulae as targets of star forming regions. The catalogued Shapeless HII regions (Sharpless 1959) from PSS served as sources for investigating gas and dust properties of molecular cloud complex (Evans, Beckwith & Blair 1977; Harvey, Campbell & Hoffmann 1977). Nearby dark cores as well as cloud fragments were from Lynds dark nebula (Strom 1975; Snell, Loren & Plambeck. 1980; Clark & Johnson 1981). After visual inspection, 70 small opaque spots were chosen for the surveys of low-mass cores with the ^{13}CO , C^{18}O and NH_3 respectively (Myers, Linke & Benson 1983; Myers & Benson 1983). A number of sources resulted in these earliest observations are still primary examples in low mass star formation so far. However, "optical dark" selection method is limited for probing star forming in the deep of molecular clouds. Bally & Lada (1983) chose infrared sources for detecting high velocity outflows in high-mass star formation regions. Particularly IRAS point sources afforded plenty samples for high mass star formation regions. Based on the similar shapes of the far infrared flux distribution of all embedded O type stars, the IRAS color-color criteria were used to choose UC HII region candidates (Wood & Churchwell 1989) and further refined by molecular line studies (Cesaroni, Walmsley & Churchwell 1992; Watson et al. 1997). Precursors of UC HII regions were also obtained from luminous IRAS sources and used for a number of surveys to examine the early characteristics of high mass star formation (Molinari et al. 1996; Sridharan et al. 2002; Beuther et al. 2002; Wu et al. 2006). In recent years, earlier samples for high mass star formation come from infrared dark clouds surveyed by MSX. These are extinction features against the bright mid-infrared background of the Galaxy (Egan et al. 1998). A number of starless massive cores were detected, which are with narrower line widths and lower rotation temperatures than both UC HII region precursors and UCHII regions but with similar masses (Rathborne, Jackson, & Simon 2006; Sridharan et al. 2005). However, MSX is limited to $|b| \leq 6^\circ$ of our Galaxy.

Now Planck Surveys provide a wealth of early sources which are cold and with unprecedented complete space distribution. The cold core Catalogue of Planck Objects (C3PO) includes 10783 sources which are mainly cold clumps, intermediate structures of the fragmentation scenario. Their temperatures and densities range from 7 to 17 K and 30 to 10^5 cm^{-3} respectively, derived from the fluxes in the three highest frequency Planck bands (353, 545, 857 GHz) and the 3000 GHz of IRAS band (Planck Collaboration. et al. 2011a). This enables us to probe the characteristics of the prestellar phase or starless clumps. The all sky nature of the Planck cold clump sample is particularly useful for studying the global properties of Galactic star formation. Follow up study with high resolution observations by Herschel Satellite revealed extended regions of cold dust with colour temperatures down to 11 K. The results show different evolutionary stages ranging from a quiescent, cold filament to clumps with star formation activities (Juvela et al. 2010).

These known properties of Planck cold clumps currently were revealed with various bands of continuum emissions and only a set of 8 C3PO sources selected from different environment (Planck Collaboration. et al. 2011b) were investigated with molecular lines. Examination with molecular lines is another essential aspect for understanding the properties of the Planck cold clumps. Molecular line studies of the Planck clumps, which are an unbiased sample of cold dust clumps in the Milky Way, will provide clues to probe a number of critical questions about clumps and star formation: What are the morphologies, physical parameters and their variations in the Galaxy? What are the initial conditions of star formation, which we do not yet know in our current state of knowledge? What are the dynamic factors in a variety of the clumps and is there any premonition of collapse? Is there any depletion and what are cold chemistry phenomena? In which environment can the cold clump exist? What is the highest Galactic latitude where stars can form? CO is the most common tool to probe molecular regions. Although there is "dark gas" which is undetected in the available CO and HI surveys (Planck Collaboration. et al. 2011c), CO is still a basic probe to address the above questions.

In this paper we report a survey of Planck cold clumps with J=1-0 lines of the ^{12}CO and its major isotopes ^{13}CO and C^{18}O using the telescope of Purple Mountain Observatory at Qinghai province in western China. Our target sources are chosen from the Early Cold Core Catalogue (ECC), which are the most reliable detections of C3PO clumps. So far we have surveyed 674 sources with single point observations and mapped a subset of ten clumps in different locations. In the next section the observations are described. In section 3 we present the results. The discussions are in section 4 and a summary is given in section 5.

2. Observations

Using the 13.7 m telescope of Qinghai Station of Purple Mountain Observatory (PMO) at De Ling Ha, the survey towards the ECC clumps with the lines of ^{12}CO (1-0) and ^{13}CO (1-0) was carried out from January to May, 2011. The half-power beam width (HPBW) at the 115 GHz frequency band is $56''$. The pointing and tracking accuracies are better than $5''$. The main beam efficiency is $\sim 50\%$. A newly installed SIS superconducting receiver with nine beam array was employed as the front end. ^{12}CO (1-0) line was observed at upper sideband (USB) and the other two lines were observed simultaneously at lower sideband (LSB). The typical system temperature (T_{sys}) in SSB mode is around 110 K and varies about 10% for each beam. An FFT spectrometer was used as the back end, which is with a total bandwidth of 1 GHz and 16384 channels. The equivalent velocity resolution is 0.16 km s^{-1} for ^{12}CO (1-0) line and 0.17 km s^{-1} for ^{13}CO (1-0) and C^{18}O (1-0) lines respectively. The Position switch (PS) mode was adopted for single point observations. The off position for each "off" source was carefully chosen from the area within 3° from the "on" source, which has no or extremely weak CO emission based on the CO survey of the Milky Way (Dame et al. 1987, 2001). For those regions without CO data, we chose the off positions based on the IRAS $100 \mu\text{m}$ images. The integration time at the on/off position is 30 s.

We also mapped ten sources which are with rather strong CO emission. On-The-Fly (OTF)

observing mode was applied for mapping observations. The antenna continuously scanned a region of $22' \times 22'$ centered on the Planck cold clumps with a scan speed of $20'' \text{ s}^{-1}$. The rms noise level was 0.2 K in main beam antenna temperature T_A^* for ^{12}CO (1-0), and 0.1 K for ^{13}CO (1-0) and C^{18}O (1-0). Since the edges of the OTF maps are rather noisy, only the central $14' \times 14'$ regions are analyzed. The OTF data were then converted to 3-D cube data with a grid spacing of $30''$. The IRAM software package GILDAS was used for the data reduction (Guilloteau & Lucas 2000).

3. Results

To make the observation with a sufficiently high elevation for the 13.7 m telescope at De Ling Ha, our samples were chosen from ECC with $\text{Dec.} \geq -20^\circ$. There are 674 sources from ECC which satisfies this criterion. The name and coordinates of the 674 clumps are listed in Table 1 (Column 1-7). One clump marked with “* *” is without detection, which needs to further check. There are 36 clumps without suitable background reference positions for the CO emission observations, which were marked with “* ” after their names and excluded in further analysis. Clumps with Latitude larger than 25° are referred as high latitude clumps. There are 41 high latitude clumps. According to Dame et al. (1987), the distributions of the detected clumps are assigned to different molecular complexes. The regions and corresponding Longitude and Latitude scopes are shown in columns 1-3 of Table 2. The fourth column of Table 2 gives number of the clumps in each complex. 673 clumps were detected to have the ^{12}CO and ^{13}CO emission, and 68% of the clumps have the C^{18}O emission. 108 additional velocity components were identified in both the ^{12}CO and ^{13}CO emission, 50% of which have C^{18}O emission. We made a Gaussian function fitting for each distinguishable velocity component of the spectral lines. The results of emissions and their physical parameters are presented in the following.

3.1. Emission components and characteristics of line profiles

Most of the observed clumps have single velocity component in CO emission. Among the 673 sources, 123 and 16 have double or possible double velocity components respectively, and 18 and 10 have three or possible three velocity components. Multiple components or blend emission were detected in 52 cold sources. The spectral line of each distinguishable component was fitted with a Gaussian function. Centroid velocity V_{lsr} , antenna temperature T_A^* and full width at half maximum ΔV (FWHM) were obtained for all the 3 CO lines, which are given at Table 3. Centroid velocity of ^{13}CO was taken as the systemic velocity of each velocity components and listed in the second column of Table 4. Dense core masses are related with molecular line widths (Wang et al. 2009). We adopted an average value of ^{13}CO line width 1.3 km s^{-1} of the nearby dark cores (Myers & Benson 1983) as a criterion to distinguish high-mass and low-mass clumps. If a clump contains one or more velocity components with the ^{13}CO line width larger than 1.3 km s^{-1} , it is considered as a candidate of high mass clumps (group H), otherwise, it is taken as a candidate for low mass clumps (group L). In some of the observed clumps, the spectral lines of the emission components depart from Gaussian profile, which probably reflect the state of gas or originates from systematic motions and star formation activities. We classify the different non-Gaussian profiles with the following characters:

BA⁺: blue profile; RA⁺: red profile; BA: blue asymmetric; RA: red asymmetric; De: possible depletion; BW: blue wing; RW: red wing; W: wings; P: pedestal; Dob: Double components; T: Three components; M.B: Multiple or Blended components.

The normalized velocity difference $\delta V = (V_{thick} - V_{thin})/\delta V_{thin}$ is applied to identify the blue- and red- profiles (Mardones et al. 1997), where V_{thick} is the peak velocity of ^{12}CO (1-0), V_{thin} and δV_{thin} are the systemic velocity of optically thin lines and the line width of optically thin lines, respectively. We use ^{13}CO (1-0) and C^{18}O (1-0) as the optically thin lines. If $\delta V < -0.25$, the line is classified as "blue profile", and if $\delta V > 0.25$, the line is classified as "red profile". The

sources with blue or red profiles are listed in Table 5. We define $\delta V(12) = (V_{thick} - V_{12})/\delta V_{thin}$ to investigate line asymmetries, where V_{12} is the center velocity of ^{12}CO (1-0). The sources with asymmetric profiles are listed in Table 6. The spectrum characteristics are denoted in the last Column of Table 3. Figure 1 presents the examples of the spectra of the J=1-0 lines of the ^{12}CO , ^{13}CO and C^{18}O with red, green and blue colors respectively, including single, double and three components and the characteristics of the spectral profiles.

3.2. Observed parameters

The histograms of the line center (peak) velocity difference between the lines of ^{12}CO and ^{13}CO ($V_{12}-V_{13}$) and those of ^{13}CO and C^{18}O ($V_{13}-V_{18}$) lines are shown in Figure 2 a) and b). The distributions (blue solid histograms) of both the $V_{12}-V_{13}$ and $V_{13}-V_{18}$ are quite symmetric around the zero, which are fitted with a normal distribution (red curve). However, their distributions are much narrower than a standard normal distribution (red curve), but have a sharp peak at zero (see Figure 2 a) and b)). 94% of the clumps have $V_{12}-V_{13}$ less than 3σ of the velocity resolution given by the spectrometer, and 98% of the clumps have $V_{13}-V_{18}$ less than 3σ of the velocity resolution. The velocity correlations between lines of ^{12}CO - ^{13}CO and ^{13}CO - ^{18}CO are shown in Figure 2 c) and d). $Y=(1.002\pm 0.001)X+(0.005\pm 0.016)$ for V_{12} (Y) to V_{13} (X) and $Y=(0.992\pm 0.005)X+(0.140\pm 0.057)$ for V_{13} (Y) to V_{18} (X) show very good correlations and the correlation coefficient is 100%. This is the first time to show the good agreement of the center velocities of the ^{12}CO and its main isotopes ^{13}CO and C^{18}O lines with such a large sample. These results show that the peak velocities of the three CO lines agree very well, and demonstrate that they originate from the same emission regions. Comparisons of Fig. 2 a) and b), Fig.2 c) and d) show that the agreement between V_{lsr} of the ^{13}CO and C^{18}O lines is better than that of the ^{12}CO and ^{13}CO lines, which may suggest that the ^{12}CO is easily affected by dynamic factors in the clump or its environment.

Since there are fewer sources with detected the C¹⁸O lines than those with the ¹³CO lines, we adopt the center velocity of the ¹³CO as the systemic velocity of the clumps in the following analysis. For the components without the ¹³CO (1-0) emission, the center velocities of the ¹²CO were adopted as the systemic velocity.

Main beam antenna temperatures of the three transitions for all the components detected were obtained. T₁₂ ranges from 0.5 - 12 K. The three clumps G209.28-19.62 (12 K), G192.54-11.56 (9.2 K) and G207.35-19.82 (8.8 K) have highest temperature, which are all located in the Orion region. Generally, the antenna temperatures of ¹³CO and C¹⁸O are also high in the ¹²CO emission strong clumps. For the above three clumps, T₁₃ and T₁₈ are 6.8, 1.4; 5.0, 0.6; and 3.1, 0.4 K respectively. The ratio of T₁₂/T₁₃ is between 1.7-1.8, showing that the ¹²CO line emissions have large opacity. The ratio of T₁₃/T₁₈ ranges between 4.5-8.3, with an average value of 6.0 which is close to the terrestrial value. However the ratio may be different in different regions, for example in the Ophiuchus complex, the antenna temperatures of the three transitions are 6.7, 4.4 and 2.5 K for G003.73+18.30 and 5.9, 4.4 and 1.4 K for G006.41+20.56. The ratio of T₁₃/T₁₈ are 1.8 and 3.1 for the two clumps respectively, much less than 5.5, suggesting where the ¹³CO lines seem optical thick. For all the detected components, the histograms of T₁₂, the ratios of T₁₂/T₁₃ and T₁₃/T₁₈ are present in Figure 3 a), b) and c) respectively. The peak of T₁₂ is around 3 K. For the ratio of T₁₂/T₁₃, the mean value is 2.2 with a standard deviation of 1.4, showing the ¹²CO (1-0) line emissions of the cold clumps are optical thick generally. The mean value of the ratio of T₁₃/T₁₈ is 3.9 with a standard deviation of 1.7.

We found all the distributions of the observed parameters as well as the derived parameters seem to skew to the right with a long tail at high value side. We try to depict their distributions with a lognormal distribution. The probability density function (PDF) of a log-normal distribution is:

$$f_X(x; \mu, \sigma) = \frac{1}{x\sigma\sqrt{2\pi}} e^{-\frac{(\ln x - \mu)^2}{2\sigma^2}}, x > 0 \quad (1)$$

where x is value of the variable, the parameters denoted μ and σ , are the mean and standard deviation, respectively, of the variable's natural logarithm. The Kolmogorov-Smirnov test (K-S test) is applied to identify whether the parameters follow a lognormal distribution. The decision to reject or accept the null hypothesis is based on comparing the P-value with the desired significance level, which is 0.05 in this paper. If the P-values from K-S test is larger than 0.05, the parameter should follow the reference distribution. The statistics and K-S test results of the parameters are summarized in Table 7.

There is a similar characteristic of the distributions of T_{12} , T_{12}/T_{13} . They are both with a power-law like long tail but can not be well described with a lognormal distribution. The tail of the distribution of T_{13}/T_{18} is less than those of T_{12} and T_{12}/T_{13} , suggesting T_{12} may be the more sensitive physical element than T_{13} and T_{18} for star formation. The distribution of T_{13}/T_{18} has a lognormal shape with P-value of K-S test as high as 0.234.

From Table 3 one can see the line widths of the emission components are narrow generally. Most of the clumps have line widths smaller than 1.3 km s^{-1} . There are 162 high mass clump candidates, among them 68 have two or more velocity components. The clumps at high latitude all are low-mass clump candidates with single component except G159.23-34.49 which is in high-mass group and with two components. Figure 4 a) presents the distributions of the FWHM of all the three lines: the mean values and the standard deviations of the three line widths are 2.0 ± 1.3 , 1.3 ± 0.8 and $0.8 \pm 0.7 \text{ km s}^{-1}$ respectively. The shapes of all the distributions are similar to each other and are lognormal distributed.

3.3. Derived physical parameters

The excitation temperature derived from radiation transfer equation is:

$$T_r = \frac{T_a^*}{\eta_b} = \frac{h\nu}{k} \left[\frac{1}{\exp(h\nu/kT_{ex}) - 1} - \frac{1}{\exp(h\nu/kT_{bg}) - 1} \right] \times [1 - \exp(-\tau)] f \quad (2)$$

here T_r is the brightness temperature corrected with beam efficiency η_b . Assuming ^{12}CO emission is optically thick ($\tau \gg 1$) and the filling factor $f=1$, the excitation temperature T_{ex} can be straightforwardly obtained. The T_{ex} is given in column 6 of Table 4. We assume the excitation temperatures of ^{13}CO and C^{18}O are the same as that of the ^{12}CO (1-0) in the following analysis. The values range from 3.9 K to 27 K, wider than the dust temperature range 7 - 17 K (Planck Collaboration. et al. 2011a). The mean value with the standard deviation is 10 ± 2.6 K, which is smaller than the mean value of the dust temperature (12.8 ± 1.6 K) based on aperture photometry with a local background subtraction by Herschel photometric observations towards 71 Planck cold fields (Juvela et al. 2012), indicating the gas maybe heated by the dust. There are 12 clumps with $T_{ex} > 17$ K. All these hottest clumps are located in the Orion and Taurus regions, showing high excitation temperature may be related to star formation conditions. 93 components with $T_{ex} < 7$ K are referred to as coldest clumps among which G093.66+04.66 (3.9 K) is in the 1st Quadrant, G098.10+15.83 (5.0 K) and G112.63+20.80 (5.8 K) are in the Cepheus. All other coldest clumps are the weaker components of the clumps with double or three emission components. The T_{ex} histogram and its lognormal fit are shown in Figure 5. It's distribution can be well fitted by a lognormal shape with P-value of K-S test as large as 0.227. But the tail of the distribution seems much smaller than that of line widths and velocity dispersions. In the following analysis T_{ex} was taken as gas kinetic temperature assumed the local thermodynamic equilibrium (LTE) holds.

Both the optical depths τ_{13} and τ_{18} at the emission peak of the corresponding lines were calculated with equation (2) assuming the filling factor $f=1$, which are listed in column 7 and 9 in Table 4. τ_{13} ranges from 0.1 to 4.1. Clumps with largest τ_{13} include : G026.45-08.02 (3.2) and G058.07+03.29 (3.2) of the 1st Quadrant; G164.94-08.57 (4.1) and G179.10-06.27 (3.9) in Taurus and G182.04+00.41 (3.8) located at Anti-center. For the ten clumps with the smallest optical depth (0.1), all of them are the minor components of the double or more component sources except G121.88-08.76. Figure 6 a) shows the histogram of τ_{13} and its lognormal fitting. The mean

value is 0.93 ± 0.56 .

The column density of a molecular line can be obtained with the theory of radiation transfer and molecular excitation as following (Garden et al. 1991):

$$N = \frac{3k}{8\pi^3 B\mu^2} \frac{\exp[hBJ(J+1)/kT_{ex}]}{(J+1)} \times \frac{(T_{ex} + hB/3k)}{[1 - \exp(-h\nu/kT_{ex})]} \int \tau_{\nu} dV \quad (3)$$

where B , μ , J are the rotational constant, permanent dipole moment, and the rotational quantum number of the lower state of the molecular transition. Column densities of the ^{13}CO and C^{18}O molecules were calculated and given in Column 8 and 10 of Table 4. The maximum C^{18}O column densities of the Planck clumps are $1.1 \times 10^{16} \text{ cm}^{-2}$ and $1.3 \times 10^{16} \text{ cm}^{-2}$ in G028.56-00.24 and G160.51-16.84 respectively and the smallest ones are $1.0 \times 10^{14} \text{ cm}^{-2}$ in G26.93-20.68 and G102.72-25.96. The column densities of the C^{18}O span a wider range than those of the nearby dark clouds (Myers, Linke & Benson 1983) which are from 3×10^{14} to $2.7 \times 10^{15} \text{ cm}^{-2}$. The different column density ranges between our sample and the nearby dark clouds may be attributed to the larger space distribution of Planck cold clumps than the nearby dark clouds.

The ^{13}CO column densities were calculated for 782 velocity components. For the 437 components with both C^{18}O and ^{13}CO column densities, the abundance ratio of X_{13}/X_{18} were calculated and listed in Column 13 of Table 4. The histogram and the lognormal distribution of X_{13}/X_{18} fitting is presented in Figure 6 b). The distribution shape of the ratio X_{13}/X_{18} is similar to that of τ_{13} . The mean value of X_{13}/X_{18} is 7.0 ± 3.8 , higher than that of the terrestrial ratio 5.5. The distribution of X_{13}/X_{18} can be well depicted by a lognormal distribution with P-value of K-S test as high as 0.388.

Molecular hydrogen column densities of each velocity component were derived according to the column densities of the ^{13}CO . The fractional abundance of $[\text{H}_2]/[^{13}\text{CO}] = 89 \times 10^4$ was adopted. We also calculated the N_{H_2} for the components without ^{13}CO emission by assuming ^{12}CO (1-0) emission to be optically thin, the excitation temperature of 10 K and $[\text{H}_2]/[^{12}\text{CO}] = 10^4$, but these components are excluded in further statistics. Figure 6 c) presents the plots of the N_{H_2}

histogram and its lognormal fitting. It spans from 10^{20} to $4.5 \times 10^{22} \text{ cm}^{-2}$, which is larger than that of the 8 sources on the average (Planck Collaboration. et al. 2011b). From Herschel follow-up observations, the peak column densities of 71 clumps range from 4×10^{20} to 7.4×10^{22} (Juvela et al. 2012), which are slightly larger than the column densities obtained in this work. The four clumps with largest ^{13}CO column density are G209.28-19.62, G028.56-00.24, G033.70-00.01 and G158.37-20.72. The N_{H_2} of G209.28-19.62 located in the Orion complex is as high as $4.5 \times 10^{22} \text{ cm}^{-2}$. G028.56-00.24 and G033.70-00.01 with N_{H_2} of 3.4 and $2.8 \times 10^{22} \text{ cm}^{-2}$ are located in the 1st Quadrant. G158.37-20.72 with N_{H_2} of $2.3 \times 10^{22} \text{ cm}^{-2}$ is in Taurus, which is at $7'$ north of NGC 1333 (Strom, Vrba & Strom 1976) and with a very red young star SSV 13 (Harvey et al. 1998). The ^{12}CO lines of all these clumps have large line widths of 2.57 - 9.35 km s^{-1} , showing the turbulence support for these clumps. The column density distribution (Figure 6 c) can not be fitted with a unique lognormal distribution, but exhibits a power-law like tail, similar to that identified from active star formation regions (Kainulainen et al. 2009), indicating that some Planck cold clumps are locate in active star forming regions.

The one dimensional non-thermal (σ_{NT}) and thermal (σ_{Therm}) velocity dispersions can be estimated as following:

$$\sigma_{NT} = \left[\sigma_{^{13}\text{CO}}^2 - \frac{kT_{ex}}{m_{^{13}\text{CO}}} \right]^{\frac{1}{2}} \quad (4)$$

$$\sigma_{Therm} = \left[\frac{kT_{ex}}{m_H \mu} \right]^{\frac{1}{2}} \quad (5)$$

where $\sigma_{^{13}\text{CO}} = \frac{\Delta V_{13}}{8 \ln(2)}$ and T_{ex} are the one dimensional velocity dispersion of the ^{13}CO (1-0) and excitation temperature, respectively. k is Boltzmann's constant, $m_{^{13}\text{CO}}$ is the mass of ^{13}CO , m_H is the mass of atomic hydrogen, and $\mu=2.72$ is the mean molecular weight of the gas. Then the three-dimensional velocity dispersion σ_{3D} can be estimated as:

$$\sigma_{3D} = \sqrt{3(\sigma_{Therm}^2 + \sigma_{NT}^2)} \quad (6)$$

The three dimensional and non-thermal velocities dispersions shown in Figure 4 b) and c) also present similar distribution as line widths. As shown in Table 7, the P-values of K-S

test for lognormal hypothesis for line widths and velocity dispersions are all much larger than 0.05, indicating their distributions can be remarkably well described by a lognormal fit. The lognormal behaviors of volume or column density in molecular clouds were frequently reported in recent observations (Ridge et al. 2006; Froebrich et al. 2007; Goodman, Pineda & Schnee 2009), which are often interpreted as a consequence of supersonic turbulence in the observed clouds (Vázquez-Semadeni 1994). From our results, the effect of supersonic turbulence in the clouds should be more likely reflected in the lognormal behaviors of the distributions of line widths and velocity dispersions than in the distributions of column density. Figure 4 d) plots the distribution for the ratios of σ_{NT} to σ_{Therm} . One can find most of the clumps have σ_{NT} larger than σ_{Therm} , indicating that turbulent motions dominate in these clouds. The shape of their ratio distribution is similar to the distributions of the FWHM of the three transitions, the σ_{3D} and σ_{NT} . But the tail part is narrower than the others, which may suggest that the thermal motions may not be as sensitive as non-thermal motions for revealing star formation activity.

3.4. Mapping results

In the ten mapped clumps, 12 velocity components were detected. Six of them have FWHM of the ^{13}CO (1-0) larger than 1.3 km s^{-1} and the other 4 belong to group L. The CO line profiles of the clump G089.64-06.59, one of the velocity components of G157.60-12.17, G179.29+04.20 and G196.21-15.50 show blue asymmetric signature, The integrated intensities are shown in the contour maps in Figure 7. The morphologies of these clumps are different. G001.38+20.94 and G180.92+04.53 show both diffuse features and dense clump. G108.85-00.80, G157.60-12.17b, and G196.21-15.50 exhibit a filamentary shape with a chain of dense clumps. G161.43-35.59 and G194.80-03.41 appear as a dumbbell also in filamentary structure. Four cores are detected in G006.96+00.89a and G161.43-35.59 respectively. G049.06-04.18 is an isolate clump while G089.64-06.59 shows a cometary-like structure. Filamentary structures are the majority among

these clumps, which is consistent with the Herschel follow-up observation results (Juvela et al. 2012). Juvela et al. (2012) also found the filaments often fragment into sub-structures. Such behavior is revealed in the gas emission too as in G006.96+00.89a shown in Figure 7..

There are 22 cores identified with 2 dimensional gaussian fits to the ten mapped sources. The physical parameters of these cores are presented in Table 8. The positions of the cores are shown as offset relative to the reference positions in column 4. Deconvolved size a and b (column 5) is the major and minor angular sizes of the cores and measured from the contours at half of the maximum intensity of the ^{13}CO (1-0) lines. The radius $R = \frac{\sqrt{ab}}{2}D$, where D is the distance, in column 6 distributes from several tenth to about 3 pc. Column 7-12 list the clump parameters: T_{ex} , N_{H_2} , velocity dispersions and volume density $n_{H_2}=N_{H_2}/2R$ respectively. Then the core mass can be derived as $M=\frac{4}{3}\pi \cdot R^3 \cdot n_{H_2} \cdot m_{H_2} \cdot \mu_g$, where m_{H_2} is the mass of a hydrogen molecule and $\mu_g=1.36$ is the mean atomic weight of the gas. Core mass calculated with LTE assumption is given in column 13. Column 14 and 15 are virial mass and the Jeans mass respectively (see next Section). The final two columns are the group and the location of the clumps. The column density of the cores ranges from 1.3 to $7.7 \times 10^{21} \text{ cm}^{-2}$. The LTE masses of the cores range from 9 to $1.5 \times 10^4 M_{\odot}$ with a median value of $110 M_{\odot}$. In the Herschel follow-up observations, the 26 identified filaments have column density ranging from 0.9 to $19.2 \times 10^{21} \text{ cm}^{-2}$ and masses ranging from 3.5 to $3.2 \times 10^3 M_{\odot}$ with a median value of $120 M_{\odot}$ (Juvela et al. 2012), which are consistent with the case of the cores in this work.

4. Discussion

4.1. The line center velocities

The well coincidence of three transitions observed towards the Planck clumps is not usual in star formation regions. Line center velocities of different molecular species could be

significant offset from the systematic velocity in active star forming regions. In the six NH_3 clumps of G084.81-01.09, the deviations between the ^{12}CO and ^{13}CO are all larger than 1 km s^{-1} (Zhang et al. 2011). V_{lsr} of the ^{12}CO deviated from that of ^{13}CO or C^{18}O are also seen in infrared dark clouds. In 61 infrared dark clouds, there are 10% sources with V_{lsr} deviation of $\gtrsim 1 \text{ km s}^{-1}$ from the ^{12}CO and the C^{18}O lines (Du & Yang 2008). The rather large discrepancy between the V_{lsr} of ^{12}CO and ^{13}CO can be also seen in the sub-millimeter clumps (Qin et al. 2008). Line center velocity difference of various molecular species may origin from molecular layers with different temperature or trace different kinematical gas layers (Bergin et al. 1997; Muller et al. 2011). The deviation between V_{13} and V_{18} of the Planck clumps also tends to be smaller than those of Myers, Linke & Benson (1983). All these suggest that the cold clumps are the quietest molecular regions found so far as a whole.

4.2. Distances of the clumps:

Distance is essential to investigate the spatial distribution and physical conditions of the clumps. Planck Collaboration, et al. (2011d) have estimated distance for 2619 C3PO clumps using various extinction signatures. They also found that there are 127 Planck cold clumps associated with IRDCs which have a kinematic distance from Simon et al. (2006). In our sample there are only 2 clumps closed to the sources of Simon et al. (2006) at the 0 latitude Galactic layer. There are certainly a part of the ECC clumps have distance estimated with extinction methods. We estimated the kinematic distances of the clumps using the V_{lsr} of the clumps which could be a comparison for those with known distance. We adopt the rotation curve of Clemens (1985) $R_{\odot}=8.5 \text{ kpc}$ and $\Theta_{\odot}=220 \text{ km s}^{-1}$ in our calculation. To see the possible physical relation of the components in clumps with double and three peaks, the distance of each component was calculated. For the clumps within the inside of the solar circle there are two solutions. The clumps are perhaps located at the front of Galactic bulk of the diffuse background, since extinction is

rising along a line of sight that crosses a dust clump (Planck Collaboration. et al. 2011a). So the near value of the distances was adopted. Among our sample there is a number of clumps located in molecular complex with known distance. Since these complexes are with rather large areas and clumps resident inside are with different V_{lsr} , the kinematic distances of the clumps within one complex are quite different. Therefore for every clump within the same complex their distances are also given out as the kinematic distances. However, in a case that a clump has ambiguity on the distance, the one close to the known distance of the complex was adopted.

The histogram of the kinematic distances is plotted in Figure 8. Distances were obtained for 741 ^{13}CO components. 51% of the components are with distances within 0.5 and 1.5 kpc. The mean value is 1.57 kpc, smaller than those associated with infrared dark clouds by Simon et al. (2006). The reason may be due to cloud properties, of which most of our clumps or components belong to low mass group and the infrared dark clouds of Simon et al. (2006) are at the first quadrant of the mid-plane and with distances between 0.7 to 7.8 kpc (Simon et al. 2006).

4.3. Physical Parameter distributions in the Galaxy

4.3.1. Excitation temperature and the ratio of line strength of ^{12}CO and ^{13}CO

Figure 9 presents the distribution of the T_{ex} and the ratio of T_{12}/T_{13} . Fig. 9 a), c) are for radial changes and b), d) for the altitude from the Galactic plane. The excitation temperature is higher than 10 K from 4 to 8 kpc. The early observations also showed the high excitation of the gas emission at the 3-7 kpc molecular ring (Goldsmith 1987 and the references there in). Around 8 kpc, T_{ex} is also larger than 10 K, which may be related to the emission of the giant molecular clouds near the Sagittarius arm. The ratio of T_{12} to T_{13} is high at $R \sim 5$ kpc, then decreases with R and has a valley between 5 - 8 kpc, then have a lowest value at ~ 6 kpc, suggesting the brightness temperature of ^{13}CO (1-0) is relatively high in this region.

Fig. 9 b) shows that excitation temperature changes with the altitude. There are two peaks, 11 and 13 K at $Z \sim 350$ pc and ~ 470 pc respectively. The changes of the ratio of T_{12}/T_{13} shown in Fig. 9 d) are rather monotone and reach the low value at $Z \sim 470$ pc, suggesting the brightness temperature of ^{13}CO is relatively high at this altitude.

4.3.2. Velocity dispersion

Variations of the velocity dispersion with the distance from the Galactic center, and the altitude from the Galactic plane are investigated. The radial variations of σ_{3D} , σ_{NT} and the ratio of $\sigma_{NT}/\sigma_{Therm}$ are plotted in Figure 10 a), c) and e) respectively. The variation of the σ_{3D} and σ_{NT} as well as the ratio of $\sigma_{NT}/\sigma_{Therm}$ with R are about the same and they reached the maximum at $R \sim 5$ kpc, which suggest that the dynamic process is most violent at the 5 kpc Galactic ring. From 6 kpc, the σ_{3D} , σ_{NT} and the ratio of $\sigma_{NT}/\sigma_{Therm}$ seem linearly increase with R, indicating turbulence becomes more violent in the outer part of the Galaxy.

Figure 10 b), d), f) present changes of the velocity dispersions σ_{3D} , σ_{NT} and the ratio of $\sigma_{NT}/\sigma_{Therm}$ with the altitude. One can see that they all decrease with the increasing of the altitude from the Galactic disk to highness 475-525 pc, showing the closer to the galactic plane, the stronger of the turbulent process. At $Z \sim 680$ pc all of them reached a minor peak. We found the clumps at this minor peak are distributed around ($l \sim 174^\circ$, $b \sim 17^\circ$) or ($l \sim 4^\circ$, $b \sim 17^\circ$), this minor peak may be concerned with the emission regions of Taurus and ρ Oph. From panel e) and f), one can see non-thermal motion dominates the line broadening. This is the first time to obtain an evidence for non-thermal line broadening from survey of the ^{13}CO (1-0) lines.

One can see that there are some differences among the radial variations of the velocity dispersion and excitation temperature. The maximum of T_{ex} -R variation is at rather high values around 4- 8 kpc and reaches maximum at 6 kpc. The T_{ex} variation is milder than that of σ_{NT}

suggesting that the gas heating and cooling occur in a wider spatial region than the turbulence.

4.3.3. ^{13}CO opacity, X_{13}/X_{18} and H_2 column density

Figure 11 a) shows the radial variation of the optical depth of the ^{13}CO (1-0) lines. The smallest value is at the 5 kpc ring. Between 5.5 and 8 kpc there is a high feature, then decreases till 14 kpc. One reason for its low valley is T_{ex} is rather high around 5 kpc (see Fig. 9 a)). Besides, its emission is relatively low comparing with that of the ^{12}CO . For example, G017.22-01.47 at $R=4.90$ kpc is $\tau_{13}=0.3$, $T_{ex}=10.1$ K and $T_{13}=0.42$ K; G033.70-00.01, $R=5.05$ kpc, $\tau_{13}=0.5$, $T_{ex}=9.2$ K and $T_{13}=1.12$ K; G028.56-00.24, $R=5.28$ kpc, $\tau_{13}=0.4$, $T_{ex}=10.9$ K, $T_{13}=1.13$ K.

The ratio of X_{13} to X_{18} presented in Figure 11 c) is rather low between 5-7 kpc and its corresponding values range from ~ 6 to 7, still higher than the terrestrial value. At 8 kpc and >10 kpc the value is near 8.

Figure 11 e) shows the radial variation of the column density of hydrogen molecules. Clearly it presents an enhancement at 5 kpc where the most dense and massive star formation regions within our Galaxy are located. Then it is almost at the similar level till outer region except at 9 kpc where there is a minor low valley. Owing to the small τ_{13} around 5 kpc (see Fig. 11 a) the column density is mainly affected by the velocity dispersion σ_{3D} or σ_{NT} shown in Figure 10. To confirm the Galactic distribution of the column density, the radial distribution of the flux density at 857 GHz dust emission detected by the Planck was plotted at Figure 11 g). The variations agree with that of the column density very well. At 9 kpc the 857 GHz flux is a little higher showing another dense structure (Goldsmith 1987 and the reference therein).

The variation of τ_{13} with altitude is shown in Figure 11 b). It exhibits a high feature between 350-550 pc and reaches its maximum at 450 pc. The change of the ratio of X_{13}/X_{18} seen in Fig. 11 d) seems to be opposite to that of τ_{13} with its lowest point at $Z=450$ pc. Fig. 11 f) presents the

variation of the molecular hydrogen column density with Z . At $Z=300$ and 500 pc, the values are higher than in the other regions. There is a low valley at $Z=450$. Combining the altitude variation of τ_{13} and the velocity dispersion of Fig. 10 b), d), f) where σ_{NT} is at low values, again showing that non-thermal line width is the major factor to determine the gas column density. Between 350 - 550 pc the flux at 857 GHz is higher too, which are consistent with the variation of N_{H_2} as a whole. These results revealed that the column density reaches the maximum at $R=5$ kpc, a low valley at $Z=450$ pc and mainly caused by non-thermal velocity dispersion, which are also not reported before.

4.3.4. *Parameters of the clumps in different molecular complexes*

For the 12 complexes included in our sample, a statistical analysis of the physical parameters was made. The corresponding average values are presented in Table 2. They display different trends: The famous star formation regions including Ophiuchs, Orion, Oph-Sgr and Taurus harbor 253 observed clumps. They have the highest excitation temperatures and column densities. The average ^{13}CO FWHM of these clumps are less than 1.5 km s^{-1} , even in Orion it is only 1.29 km s^{-1} , suggesting that low mass clumps are the dominant sources in the Planck cold clumps. Their non-thermal velocity dispersion is almost two times of the thermal one except in Ophiuchs where $\sigma_{thermal} \sim \sigma_{NT}$. Cepheus harbors 87 observed clumps. The FWHM of ^{13}CO J=1-0 line is between Orion and the above mentioned star formation regions. σ_{NT} is also the dominant factor for the line broadening. A common character can be seen that all the 4 Quadrants and the anti-center regions have FWHM of ^{13}CO J=1-0 line $\gtrsim 1.5 \text{ km s}^{-1}$. All of them belong to the high mass group. The σ_{NT} is about 4 times of the $\sigma_{thermal}$, indicating that these regions have stronger dynamic processes than other star formation regions.

4.4. Line profiles

There are 15 clumps having absorption dip at the line center, which is rather symmetric relative to the V_{lsr} . Eight of them show the dip in all the three transitions. They may be the candidates for the ^{12}CO depletion. In the other 7 clumps, only ^{12}CO line has the center dips which may originate from self-absorption. Mapping is needed to further examine the properties of the line center dips. 18 and 15 cores were identified have blue and red profiles (see Table 5). Blue profiles are a kind of typical feature of molecular clump collapse (Zhou et al. 1993). While the red profile could originate from expansion of the clump or outflow motion. The ratios of the clump with the blue and red profiles to the total clump numbers of clumps are small, which are 2.7% and 2.2% respectively. The blue excess $E = (N_b - N_r)/N_t$ is 0.004, here N_b , N_r and N_t are the clump numbers with the detected blue and red profiles and the surveyed sample (Mardones et al. 1997). E of the Class -I, 0 and I clumps is 0.31, 0.30 and 0.30 shown in HCN (3-2) line respectively (Evans 2003) while it is 0.15-0.17 for UC HII region precursors and 0.58 for UCHII regions detected with $\text{HCO}^+(1-0)$ lines (Wu et al. 2007; Fuller, Williams, & Sridharan 2005). Nevertheless a sample of 27 Orion starless clumps, 9 have blue profile and 10 have red one, implying that the blue excess E is -0.04 (Velusamy et al. 2008). The ratios of blue and red profiles to these cores are 33% and 37%, greatly exceeding those of our sample, suggesting that star formation activities occur more frequently in the Orion cores than in the Planck cold clumps. The small ratio of the blue and red profiles means that most of the Planck cold clumps do not have systematic star forming motion yet. We also identified 19 and 13 cores with blue and red line asymmetry respectively. Different from blue and red profile, line asymmetry reflects whole gas motion of the core, which may results in interaction of the core and its environment.

The high velocity wings are rare in Planck cold clumps. Among the surveyed clumps, only 3 clumps were detected with blue wing and 6 with red one, 8 with both blue and red wings and 5 with pedestal feature, showing rather rare star formation feed back activities.

4.5. Conditions of the clumps at high latitude clumps

There are 41 clumps located at latitude higher than 25° . Six clumps have two velocity components and one has three. Five of the clumps belong to the high mass group. T_{ex} is intermediate among the 12 complexes (see Table 2). The column density is $3 \times 10^{21} \text{ cm}^{-2}$ on the average. σ_{NT} tends to be smaller among the 12 complexes but still larger than those in the Ophiuchs and Oph-Sgr. Core G089.03-41.28 is with blue profile while cores G182.54-25.34 and G210.67-36.77 are with red profile. Their altitudes are 2.4, 0.64 and 0.15 kpc respectively, showing that star formation signatures also exist in clumps at high latitude. Here the kinematic distance was adopted.

Since the diffuse emission was found over all the Galactic sky (Hauser et al. 1984), many high latitude clouds such as infrared cirrus were also detected (Low et al. 1984). Heithausen et al. (1993) made a survey for $16^\circ \leq b \leq 44^\circ$, $117^\circ \leq l \leq 160^\circ$ in the 2nd quadrant. They found that the clouds with the CO emission are 13% of the survey sample. Yamamoto et al. (2003) also carried out a CO survey within the latitude -30° - (43°) . They identified 110 ^{12}CO clouds with a total of mass of $1200 M_\odot$, in which all of the clouds are not dense enough to form stars. The conditions of our 41 Planck samples are more closer to star forming statues. Additionally the latitudes of the Planck clumps exceed the above samples. These results suggest that the ECC clumps are a good guide to investigate initial conditions or search for star formation.

4.6. States of the ten mapped clumps:

The different morphologies of the contour maps of the ten mapped clumps show that the Planck clumps contain a rather long evolutionary sequence, which includes diffuse and elongating regions, filament structure or cometary shape, multiple cores as well as isolated core.

Assuming a core is a gravitationally bound isothermal sphere with uniform density and

is supported solely by random motions, the virial mass M_{vir} can be calculated following Ungerechts et al. (2000):

$$\frac{M_{vir}}{M_{\odot}} = 2.10 \times 10^2 \left(\frac{R}{pc}\right) \left(\frac{\Delta V}{km\ s^{-1}}\right) \quad (7)$$

where R is the radius of the clump and ΔV is the line width of the ^{13}CO (1-0). The virial masses are listed in the column 14th of Table 8.

In molecular clouds, many factors including thermal pressure, turbulence, and magnetic field support the gas against gravity collapse. The Jeans mass, which takes into account of thermal and turbulent support, can be expressed as (Hennebelle & Chabrier 2008):

$$M_J \approx 1.0 a_J \left(\frac{T_{eff}}{10\ K}\right)^{3/2} \left(\frac{\mu}{2.33}\right)^{-1/2} \left(\frac{n}{10^4\ cm^{-3}}\right)^{-1/2} M_{\odot} \quad (8)$$

where a_J is a dimensionless parameter of order unity which takes into account the geometrical factor, $\mu = 2.72$ is the mean molecular weight, $n = \frac{N_{H_2}}{2R}$ is the volume density of H_2 and $T_{eff} = \frac{C_{s,eff}^2 \mu m_H}{k}$ is the effective kinematic temperature. The effective sound speed $C_{s,eff}$ including turbulent support can be calculated as:

$$C_{s,eff} = [(\sigma_{NT})^2 + (\sigma_{Therm})^2]^{1/2} \quad (9)$$

The calculated Jeans masses are listed in the 15th column of Table 8.

There are 7 cores with M_{LTE} larger than M_{vir} and M_J , which maybe under collapse. There are also 7 cores having M_{LTE} agree M_{vir} and M_J within a factor of three. Considering the uncertainties in mass estimation, these cores may be in magical states. The remaining cores seem to be gravitationally unstable. One should keep in mind, these ten clumps are not a representative sample for the whole ECC, but include the morphologies of the majority of the Planck clumps. Most of the ECC clumps show diffuse molecular emission or harbor gravitationally stable dense cores (Liu, Wu & Zhang, in preparation).

The mapped clumps are noted individually as the following:

G001.38+20.94: It is located in ρ Oph. The gas emission is diffuse and with size >1 pc. The density is lower than 10^3 cm^{-3} and mass $>750 M_{\odot}$. The excitation temperature is rather high (14 K). The average σ_{3D} is only 0.67 km s^{-1} . Actually it is located at (0.5,-1.0) with respect to L43B, the mixture of isolated globules and complex (Benson & Myers 1989). Maybe it is in the transition between diffuse ISM and dense molecular cloud.

G006.96+00.89: It is located in the 4th quadrant. Two velocity components with V_{lsr} 9.33 and 41.67 km s^{-1} were detected in the clump and both have FWHM larger than 1.3 km s^{-1} . The two velocity components have 4 and 1 cores respectively. No astronomical object was found associated with this clump so far. G006.96+00.89a with 4.33 km s^{-1} velocity component appears elongated from SE to NW and has a chain of at least four cores. The other component has an isolated core near the mapping center, and the cores are not very dense with n lower than 10^3 cm^{-3} .

G049.06-04.18: It is an isolated clump and located in the first quadrant. The mass calculated with LTE is close to the Jeans and virial mass. It is CB 198 and contains IRAS 19342+1213 (J2000=19 36 37.8 +12 19 59) located at (8'', 43'') of the clump (Gómez et al. 2006).

G089.64-06.59: It is a clump of the first quadrant. Its gas clump tends to be cometary. The starless clump CB 232 AMM 1 is located at (20'', -36'') of the clump. It harbors an infrared source IRAS 21352+4307 (Huard, Sandell, & Weintraub 1999). At about 15'' eastern there is a near infrared source YC1-I. The LTE mass and the Jean mass, virial mass all are close to each other.

G108.85-00.80: It belongs to the 2nd quadrant. There are no associated objects or known cloud was found for this clump. It shows a filamentary structure and is compact. The ^{13}CO (1-0) line width is 2.7 km s^{-1} and is a typical high mass clump. The LTE mass is larger than both the Jeans and virial mass. It seems very likely to be in gravitational collapse.

G157.60-12.17: It locates in the Taurus complex and has two components belonging to L

group. Contours of their integrated intensity show the first component is rather diffuse and the second one contains two cores. TGU 1064 is located at 65'' east and south (Dobashi et al. 2005).

G161.43-35.59: It is a high latitude clump and belongs to L group. It contains at least 4 cores. No associated object was found.

G180.92+04.53: It is at the side of Anticenter of the Galaxy and belongs to the H group.

G194.80-03.41. The dumbbell gas emission region elongates in north-west direction. Two large clumps are connected and each contains at least two cores. There was no associated object found. All the cores should be starless. The clump masses are all larger than the corresponding Jean and virial mass, suggesting they are at the gravitational bound states. TGU H1364 P8 is about 2' away (Dobashi et al. 2005).

G196.2-15.5: This clump is with blue asymmetry line (see Table 6). It is associated with L1595 and a reflection nebular VDB 40 (Maddalena et al. 1986). Three cores were found in this filamentary structure. All belong to Group L. Except the $M_J < M_{LTE}$, for the core 1, M_{LTE} is less than M_J and M_{vir} , but all these masses are close to each other.

The morphology, structure and physical parameters of the small set of the ten mapped clumps show that Planck cold clumps cover different phases which may be 1: in a transition phase from diffuse ISM to cloud; 2: in a state close to gravitational bound. Among the 10 clumps, 4 are in filamentary or elongated shape which show that filamentary clumps may be the majority in C3PO clumps. 3: an isolated core or multiple cores; 4: starless cores, 5: in a state that harbor infrared sources. In total 22 cores were found and 20 are starless.

4.7. Gas and dust coupling

The range of the clump kinetic temperature is from 4-27 K, wider than those of dust temperatures (7-17 K) (Planck Collaboration. et al. 2011a). However there are only 12 clumps with $T_k > 17$ K. The ~98% clumps have $T_k \leq 17$ K, showing both the dust and gas are cold and couple well. Figure 12 a) shows a comparison of the T_k and T_d in both "Total" and "Cold" (see Fig. 12 a)). Most of the clumps are with $T_d > T_k$, indicating that gas could be heated by dust in these regions (Goldreich & Kwan 1974). For the clumps with $T_d < T_k$, the gas may be due to ongoing protostellar process. For example, for the 27 clumps with $T_k > 16$ K $> T_d$, 6 are in or close to Ophiuchus, 8 in Taurus and 10 in Orion. The column densities deduced from dust emission and CO lines were plotted in Figure 12 b). One can see that the range of the values from dust is about 3 orders in total and that from CO lines is about 2.5 orders, slightly narrower. However both the column densities concentrate on 10^{21} - 10^{22} cm⁻². According to Hartquist & Williams (1998) such column density is just about the critical value of the cloud collapse.

4.8. Evolutional phases - A comparison to different star formation samples

To investigate the physical conditions and examine the possibility of stars forming in the cold clumps, we compare the line widths of ¹³CO (1-0) and column densities with the following CO molecular line surveys towards different kind of targets:

- a) Methanol maser sources (Liu, Wu & Wang 2010);
- b) Candidates of UC HII region chosen with the IRAS colour index and flux limit (Wu, Wu & Wang 2001; Wood & Churchwell 1989);
- c) Candidates of extremely young stellar objects chosen with redder color IRAS index and smaller flux density than those of UC HII regions (Wang et al. 2009);

d) Infrared dark clouds (IRDCs) (Simon et al. 2006).

e) Extended green objects (EGOs) identified from the Spitzer GLIMPSE survey (Chen et al. 2010)

Figure 13 a) plots a cumulative fraction of the FWHM of ^{13}CO (1-0). It shows that the methanol maser sources have the largest FWHM and the smallest slope. And the IRDCs and EGOs have similar shape with the methanol maser sources but with a slightly larger slope. When the FWHM is less than 3 km s^{-1} , the slope of IRDCs is almost the same as those of the UC HII candidates and the redder-weaker IRAS sources. When FWHM becomes larger than 3 km s^{-1} , the changes of the the UC HII candidates and the redder-weaker IRAS sources are much steeper than IRDCs, EGOs and the methanol maser sources. The slope of the fraction of the redder-weaker IRAS is large and its maximum value is at 6 km s^{-1} . The variation of cumulative fraction function of FWHM for the Planck cold clumps is the narrowest. The FWHM of the Planck cold clumps are the smallest comparing with the other samples. For all the samples used in the comparison with Planck cold clumps, their FWHM are almost larger than 2 km s^{-1} while the cumulative fraction at $\text{FWHM} > 2 \text{ km s}^{-1}$ of the cold clumps is less than 10%.

The comparison of column densities with the samples of the above a), c), d) and e) is presented in Figure 13 b). The cumulative fraction distribution also produces the smallest column density range for the Planck cold clumps. IRDCs have nearly the same shape with Planck cold clumps when column density below 10^{21} cm^{-2} , but are similar with the redder-weaker IRAS sources at high densities, indicating IRDCs may be at a transition phase between Planck cold clumps and redder-weaker IRAS sources. The methanal maser sources and EGOs have the largest column densities, indicating active star formations in them.

These results show that the Planck cold clumps are quiescent and have smallest column densities among these star formation samples on the whole. Most of them seem to be in transition from clouds to dense clumps.

5. Summary

Aiming to understand gas properties of the Planck cold dust clumps we have carried out a survey for ECC clumps with J=1-0 lines of the ^{12}CO , ^{13}CO and C^{18}O . Using the 13.7 m telescope of PMO, 674 clumps were observed. Their observed parameters V_{lsr} , FWHM and antenna temperature were presented. Distances and physical parameters T_{ex} , velocity dispersions and N_{H_2} were derived, and their spatial distribution, regional difference and environmental effect were investigated. Ten clumps were mapped and their morphologies and properties were analyzed. Evolutionary states of the cold clumps were discussed when comparing with different star formation samples. Our main findings are as following:

1. With the survey of the 673 clumps, 782 ^{13}CO emission components were identified. 437 components have the detection of all the three transitions. Line center velocity differences for $V_{12}-V_{13}$ of 94% clumps and for $V_{13}-V_{18}$ of 98% clumps less than 3σ of the velocity resolution. The correlations between the V_{12} and V_{13} , V_{13} and V_{18} have $\sim 100\%$ confidence. This is the first time to confirm the agreement of the velocities of the ^{12}CO and its major isotopes ^{13}CO and C^{18}O lines at such a large sample. It suggests that the Planck clumps are quite, cold and uniform as a whole and have no significant differences in dynamical or thermal material layer structures.

2. For each of the identified components, kinematic distances, galactocentric distance and altitude from the galactic plane were derived. The distance ranges from 0.1 to 21.6 kpc and 82% of them are located within 2 kpc and 51% of the components have distances within 0.5 and 1.5 kpc.

3. The mean value of ^{12}CO antenna temperature T_{12} is 3.08 ± 1.37 K. Mean ratio of T_{12}/T_{13} is 2.15 ± 1.35 and T_{13}/T_{18} is 3.88 ± 1.71 . Excitation temperature ranges from 3.9-27.0 K. 98% of the clumps have T_{ex} (or T_k under LTE assumption) smaller than 17 K. A comparison of the T_k and T_d shows that most of the clumps are with $T_d > T_k$ suggesting gas could be heated via collision with dust and dust and gas are coupled well in 95% of the clumps. There are clumps with $T_k > 17$ K,

which are located in star formation regions such as the Orion and Taurus, suggesting that the high T_k is related to star forming activities.

4. The mean FWHM of the three transitions are 2.03 ± 1.28 , 1.27 ± 0.77 , 0.76 ± 0.75 respectively. Adopting 1.3 km s^{-1} of the FWHM of the ^{13}CO (1-0) lines as a criterion of high or low mass clumps, there are $\sim 75\%$ belonging to L Group, suggesting that the majority of the ECC clumps are low mass clumps. For the ^{13}CO lines three dimension velocity dispersion σ_{3D} , non-thermal velocity dispersion σ_{NT} were calculated and it is found that the non-thermal motion is dominant line broadening.

5. Column densities of the ^{13}CO and C^{18}O were derived. They span from 10^{14} - 10^{16} cm^{-2} , which are about critical value for collapse. The ratio of $[\text{X}_{13}]/[\text{X}_{18}]$ has mean value 7.0 ± 3.8 , higher than the terrestrial value. Hydrogen molecule column densities were obtained for 782 ^{13}CO components, which are from 10^{20} to $4.5 \times 10^{22} \text{ cm}^{-2}$. Column densities derived from CO observations cover narrower range than those deduced from dust emission.

6. Histograms for antenna temperature T_{12} , ratio of T_{12}/T_{13} , T_{13}/T_{18} , excitation temperature T_{ex} , and the velocity dispersions (σ_{3D} , σ_{NT} and ratio of $\sigma_{NT}/\sigma_{therm}$) as well as τ_{13} , $[\text{X}_{13}]/[\text{X}_{18}]$ and N_{H_2}) were fitted with lognormal distribution. The distributions of line widths of the three transitions, T_{13}/T_{18} , T_{ex} , σ_{3D} , σ_{NT} , $\sigma_{NT}/\sigma_{therm}$ and $[\text{X}_{13}]/[\text{X}_{18}]$ can be well depicted purely by a lognormal distribution. We found that the deviation of the N_{H_2} cumulative fraction distribution from the lognormal distribution originates from that of optical depth. The long tail of the distribution of the column density is consistent with those found in active star forming regions, indicating some of the Planck cold clumps reside in star forming regions. We suggest the distributions of line widths or velocity dispersions are more likely to reflect the effect of supersonic turbulence in clouds.

7. Physical parameters variations in Galactic space were investigated. As a variation with radial the hydrogen molecule column density reaches the maximum at $R \sim 5 \text{ kpc}$, which is

consistent with the 857 GHz flux density. However τ_{13} decreases to a low valley while the σ_{NT} or σ_{3D} reach the peak. The results suggest that the velocity dispersion of the molecular line is the dominant factor in determining the column density. Velocity dispersions decrease with the Altitude increase and reach the lowest point at $Z=450$ pc. Although τ_{13} is at its highest value here, the column density is at a low valley, further conforming that non-thermal line broadening plays a major role in exciting the molecular transition.

8. Line profile characteristics including possible depletion dip, blue and red profiles as well as high velocity wings were found in part of the clumps, indicating the star forming activities. However the number of these clumps less than 10% of the whole sample, indicating that star formation is not active yet in Planck cold clumps.

9. Parameters in different molecular complexes in our Galaxy show different scores. Clumps in molecular complex Ophiuchs, Taurus and Orion show high excitation temperatures while those in 1st-4th quadrants have larger velocity dispersions.

10. Ten mapped cold dust clumps have very different gas emission morphologies, showing that filaments and elongated structures are in the majority. 22 gas cores were identified with size tenth to 5 pc, density from 10^2 - 10^3 cm^{-3} and mass from dozens to thousands of M_{\odot} . Only 7 cores seem to be in gravitational bound state.

11. Planck cold clumps are the most quiescent ones among the samples of weak-red IRAS, UC HII candidates, IRDCs, EGOs and methanol maser sources, suggesting that the Planck cold clumps are at the very early phase in cloud evolution.

This work is a preliminary investigation for Planck cold clumps. Mapping observations are necessary for obtaining properties of the Planck clumps. Various molecular species, especially dense molecular tracers are needed for examining dense clumps and star formation processes in the ECC clumps. Mapping with HI line in ECC clumps is useful to investigate the transition from

diffuse to dense ISM.

Acknowledgment

We are grateful to the staff at the Qinghai Station of PMO for their assistance during the observations. Thanks for the Key Laboratory for Radio Astronomy, CAS for partly support the telescope operating. This work was partly supported by China Ministry of Science and Technology under State Key Development Program for Basic Research (2012CB821800).

REFERENCES

- Bally, J. & Lada, C. J., 1983, ApJ, 265, 824
- Benson, P. J. & Myers, P. C., 1989, ApJS, 71, 89
- Bergin, E. A., Ungerechts, H., Goldsmith, P., F. et al. 1997, ApJ, 482, 267
- Beuther, H., Schilke, P., Menten, K. M., et al. 2002, ApJ, 566, 945
- Cesaroni, R., Walmsley, C. M., & Churchwell, E., 1992, A&A, 256, 618
- Chen, Xi., Shen, Z.-Q., Li, J.-J., Xu, Y., & He J.-H., 2010, ApJ, 710, 150
- Clemens, D. P. 1985, ApJ, 295, 422
- Clark, F. O., & Johnson, D. R., 1981, ApJ, 247, 104
- Dame, T. M., Ungerechts, H., Cohen, R. S. et al. 1987, ApJ, 322, 706
- Dame, T. M., Hartmann, D., & Thaddeus, P., 2001, ApJ, 547, 792
- Dobashi, K., Uehara, H., Kandori, R. et al. 2005, PASJ, 57, 1
- Du, F. J., & Yang, J., 2008, ApJ, 686, 384
- Egan, M. P., Shipman, R. F., Price, S. D., Carey, S. J., & Clark, F. O. 1998, ApJ, 494, L199
- Evans, N. J., II., Beckwith, S., Blair, G. N., 1977, ApJ, 217, 448
- Evans, N. J., II. 2003, in Chemistry as a Diagnostic of Star Formation, ed. C. L. Curry & M. Fich (Ottawa: NRC Press), 157
- Froebrich D., Murphy G. C., Smith M. D., Walsh J., Del Burgo C., 2007. MNRAS, 378, 1447
- Fuller, G. A., Williams, S. J., & Sridharan, T. K. 2005, A&A, 442, 949
- Garden, R. P., Hayashi, M., Hasegawa, T., Gatley, I., Kaifu, N., 1991, ApJ, 374, 540

- Gómez, JoséF., de Gregorio-Monsalvo, I., Suárez, O., Kuiper, T. B. H., 2006, 132, 1322
- Goldreich, P., & Kwan, J., 1974, ApJ, 189, 441
- Goodman A. A., Pineda J. E., Schnee S. L., 2009, ApJ, 692, 91
- Guilloteau, S. & Lucas, R., 2000, in Astronomical Society of the Pacific Conference Series, Vol. 217, Imaging at Radio through Submillimeter Wavelengths, ed. J. G. Mangum & S. J. E. Radford, 299
- Hartquist, T., Caselli P., Rawlings J., Ruffle D., & Williams, D., 1998, The Chemistry of Star Formation Regions, in the Molecular Astrophysics of Stars and Galaxies, T.Hartquist, D. Hartquist, eds., Oxford:Clarendon,p.101
- Harvey, P. M., Campbell, M. F., Hoffmann, W. F., 1977, ApJ, 211, 786
- Harvey, P. M., Smith, B. J., di Francesco, J., Colome, C., 1998, ApJ, 499, 294
- Hauser, M. G., Gillett, F. C., Low, F. J. et al. 1984, ApJ, 278, L15
- Heithausen, A., Stacy, J. G., de Vries, H. W., Mebold, U., Thaddeus, P., 1993, A&A, 268, 265
- Hennebelle, P., & Chabrier, G., 2008, ApJ, 684, 395
- Huard, Tracy L., Sandell, Göran., & Weintraub, David A., 1999, ApJ,526 ,833
- Juvela, M., Ristorcelli, I., Montier, L. A. et al. 2010, A&A, 518, L93
- Juvela, M., Ristorcelli, I., Pagani, L. et al. 2012, arXiv: 1202.1672
- Kainulainen J., Beuther H., Henning T., Plume R., 2009, A&A, 508, L35
- Lee, Chang Won., & Myers, Philip C., 1999, ApJS, 123, 233
- Liu, T., Wu, Y., & Wang, K., 2010, RAA, 10, 67
- Low, F. J., Young, E., Beintema, D. A. et al. 1984, ApJ, 278, L19

- Maddalena, R. J., Morris, M., Moscowitz, J., Thaddeus, P., 1986, *ApJ*, 303, 375
- Mardones, D., et al. 1997, *ApJ*, 489, 719
- Molinari, S., Brand, J., Cesaroni, R., & Palla, F. 1996, *A&A*, 308, 573
- Muller, S., Beelen, A., Guélin, M. et al. 2011, *A&A*, 535, 103
- Myers, P. C., Linke, R. A., & Benson, P. J., 1983, *ApJ*, 264
- Myers, P. C. & Benson, P. J., 1983, *ApJ*, 266, 309
- Planck Collaboration., Ade, P. A. R., Aghanim, N., Arnaud, M. et al. 2011a, arXiv:1101.2035
- Planck Collaboration., Ade, P. A. R., Aghanim, N., Arnaud, M. et al. 2011b, arXiv:1101.2034
- Planck Collaboration., Ade, P. A. R., Aghanim, N., Arnaud, M. et al. 2011c, *A&A*, 536, 19
- Planck Collaboration., Ade, P. A. R., Aghanim, N., Arnaud, M. et al. 2011d, *A&A*, 536, 23
- Qin, S.-L., Huang, M., Wu, Y., Xue, R., Chen, S., 2008, *ApJ*, 686, L21
- Rathborne, J. M., Jackson, J. M., & Simon, R., 2006, *ApJ*, 641, 389
- Ridge N. A. et al., 2006, *AJ*, 131, 2921
- Sharpless, S., 1959, *ApJS*, 4, 257
- Simon, R., Rathborne, J. M., Shah, R. Y., Jackson, J. M., Chambers, E. T., 2006, *ApJ*, 653, 1325
- Snell, R. L., Loren, R. B., Plambeck, R. L., 1980, *ApJ*, 239, L17
- Sridharan, T. K., Beuther, H., Schilke, P., Menten, K. M., & Wyrowski, F. 2002, *ApJ*, 566, 931
- Sridharan, T. K., Beuther, H., Saito, M., Wyrowski, F., Schilke, P., 2005, *ApJ*, 634, L57
- Strom, K. M., Strom, S. E., Carrasco, L., Vrba, F. J., 1975, *ApJ*, 196, 489
- Strom, S. E., Vrba, F. J., & Strom, K. M., 1976, *AJ*, 81, 314

Ungerechts H., Umbanhowar P., & Thaddeus P., 2000, ApJ, 537, 221

Vázquez-Semadeni E., 1994, ApJ, 423, 681

Velusamy, T., Peng, R., Li, D., Goldsmith, P. F., Langer, William D., 2008, ApJ, 688, L87

Wang, K., Wu, Y, Ran, L., Yu, W. T., Miller, M., 2009, A&A, 507, 369

Watson, Alan M., Coil, Alison L., Shepherd, Debra S., Hofner, Peter, Churchwell, Ed., 1997, ApJ, 487, 818

Winnewisser, G., Churchwell, E., Walmsley, C. M., 1979, A&A, 72, 215

Wood, Douglas O. S. & Churchwell, Ed., 1989, ApJ, 340, 265

Wu, Y., Wu, J., Wang, J., 2001, A&A, 380, 665

Wu, Y., Zhang, Q., Yu, W. et al. 2006, A&A, 450, 607

Wu, Y., Henkel, C., Xue, R., Guan, X., Miller, M., 2007, 669, L37

Yamamoto, H., Onishi, T., Mizuno, A., Fukui, Y., 2003, ApJ, 592, 217

Zhang, S. B., Yang, J., Xu, Y. et al. ApJS, 193, 10

Zhou, S., Evans, N. J. II, Koempe, C., & Walmsley, C. M. 1993, ApJ, 404, 232

b

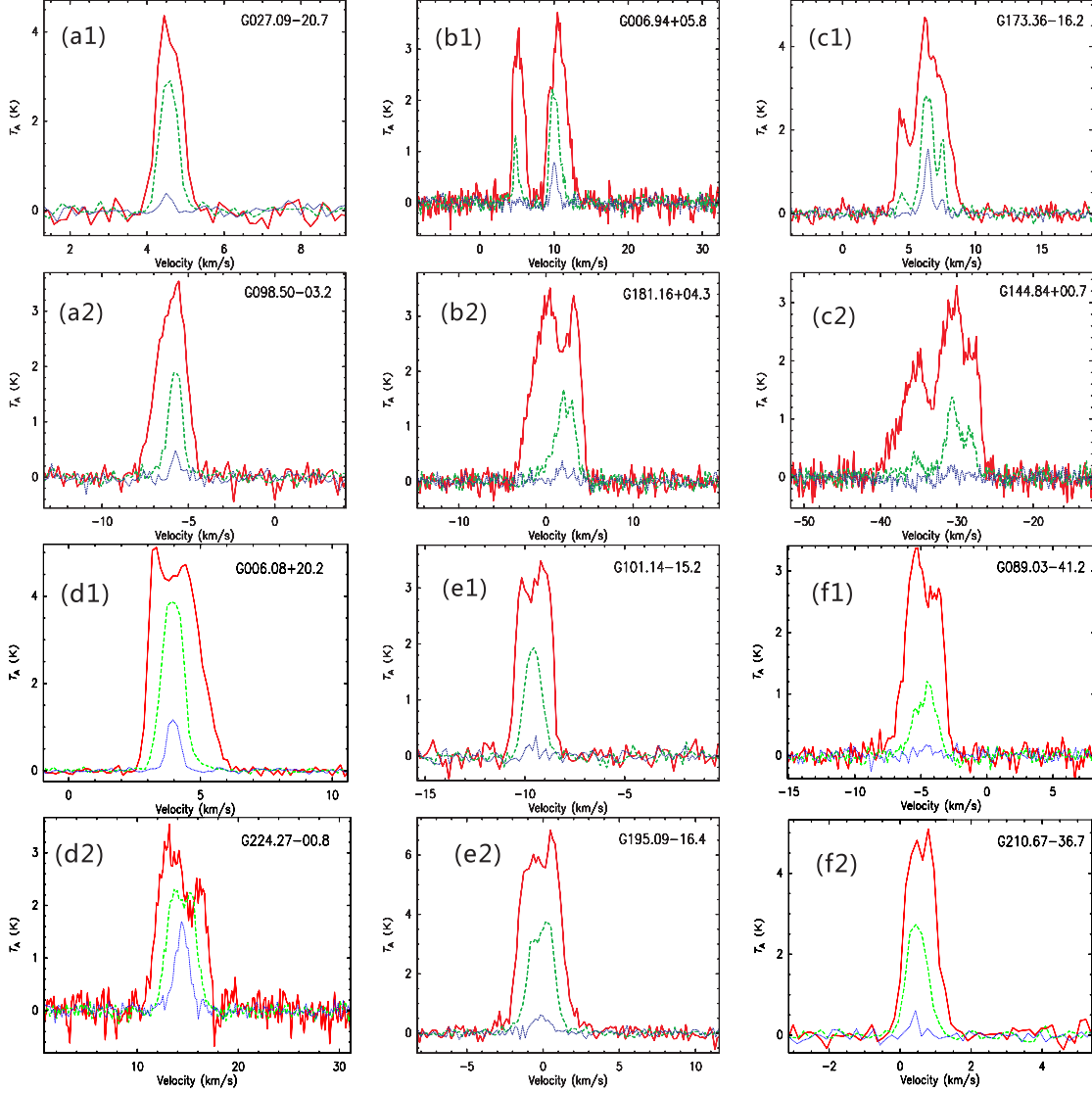


Fig. 1.— Examples of J=1-0 lines of ^{12}CO , ^{13}CO and C^{18}O spectra with different profiles. The classes are as following: a, b, c denote single, double and three velocity component spectrum respectively. d,e for blue- and red- profile; "1" and "2" for low and high mass group respectively. f1 and f2 for blue and red profile of high latitude clumps. g,h,i, for blue-, red-asymmetry and center dip respectively; j, k, and l for blue wing, red wing and pedestal respectively, "1" and "2" denote the same as above.

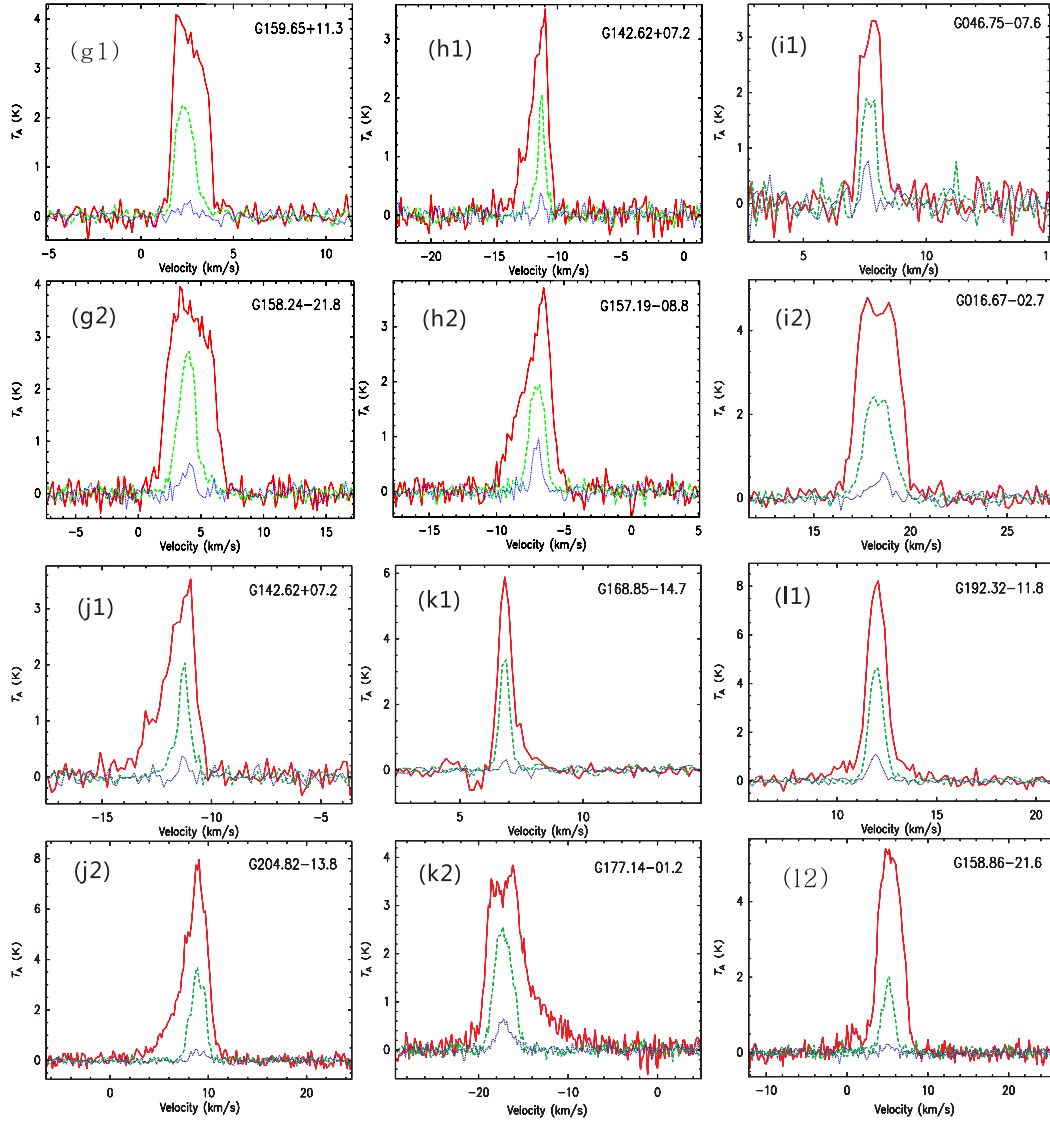


Fig. 1.— continued

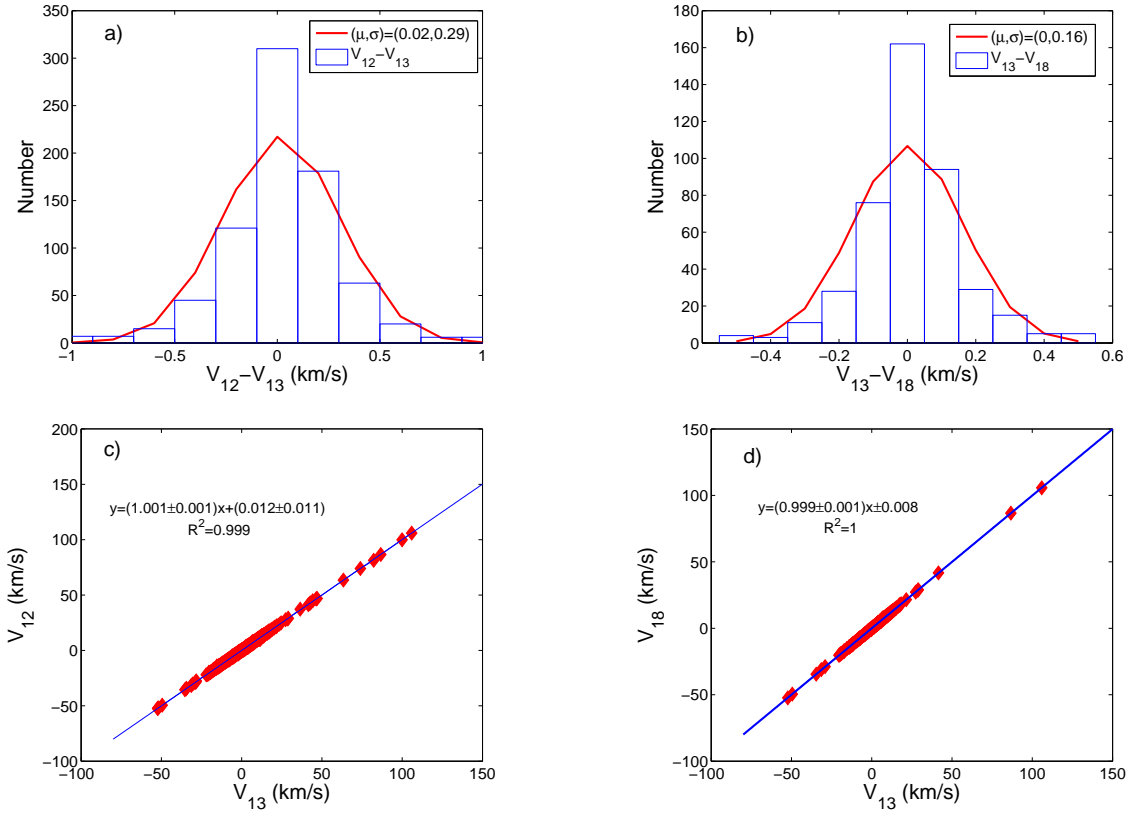


Fig. 2.— Line center velocities of the J=1-0 lines of ^{12}CO , ^{13}CO and C^{18}O : a) and b) the histogram and the normal distribution fits for the difference between V_{12} and V_{13} , V_{13} and V_{18} respectively. The mean μ and standard deviation σ of the normal distributions are presented in the upper-right boxes; c) and d): plots for V_{12} vs. V_{13} and V_{13} vs. V_{18} respectively.

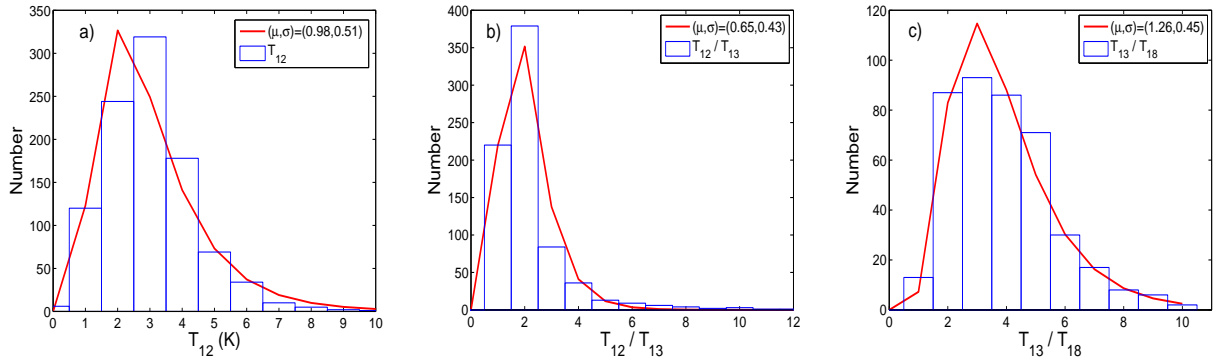


Fig. 3.— The frequency distributions of antenna temperature T_{12} , the ratio of T_{12}/T_{13} and T_{13}/T_{18} .

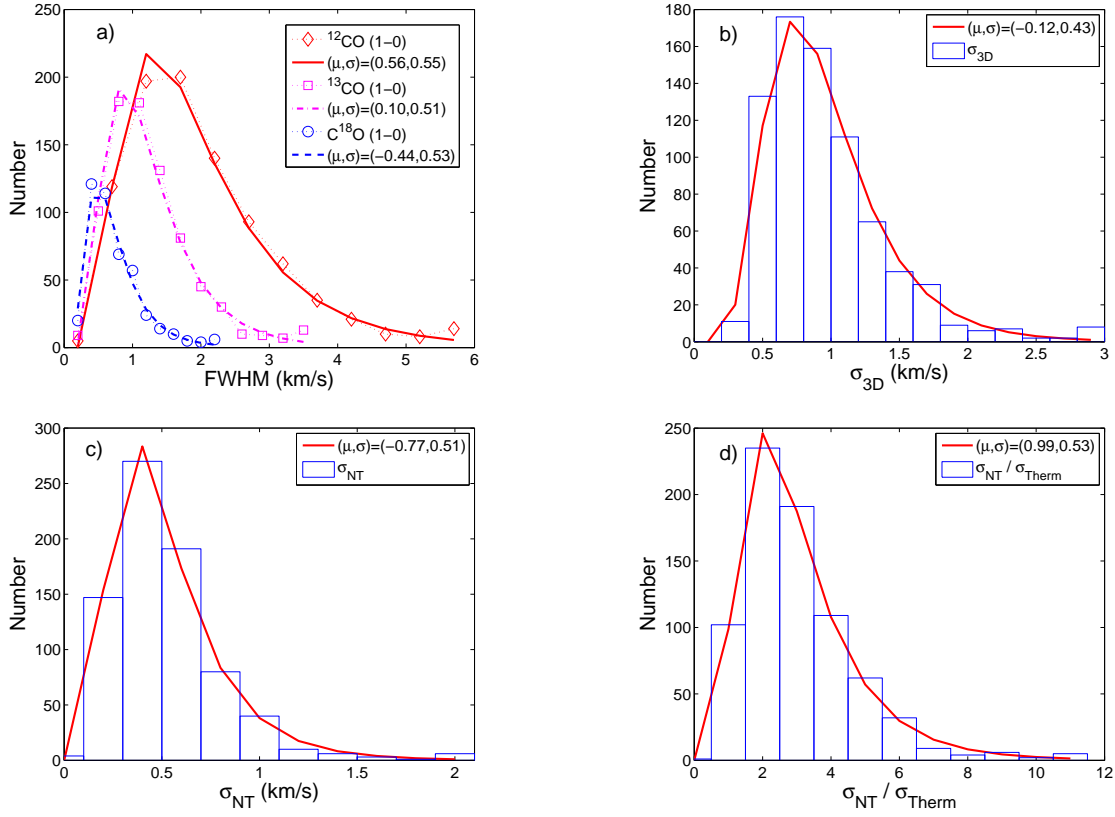


Fig. 4.— The frequency distributions of line FWHM and velocity dispersion: a). Distributions and lognormal fitting of FWHM of the CO, ^{13}CO and C^{18}O lines; b) Histogram and the lognormal fitting of the ^{13}CO line 3D velocity dispersion; c) Velocity dispersion of non-thermal motion ^{13}CO lines; d) Histogram and lognormal fitting of ratio of the ^{13}CO line non-thermal and thermal motion. The mean μ and standard deviation σ of the lognormal distribution fits are presented in the upper-right boxes in each panel.

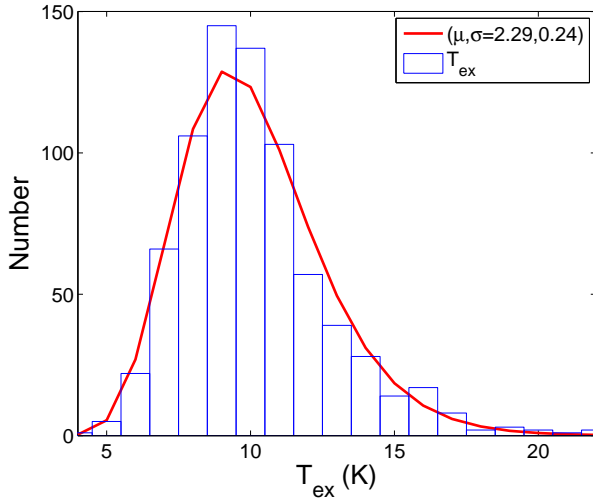


Fig. 5.— The histogram and the lognormal-PDF fitting of excitation temperatures

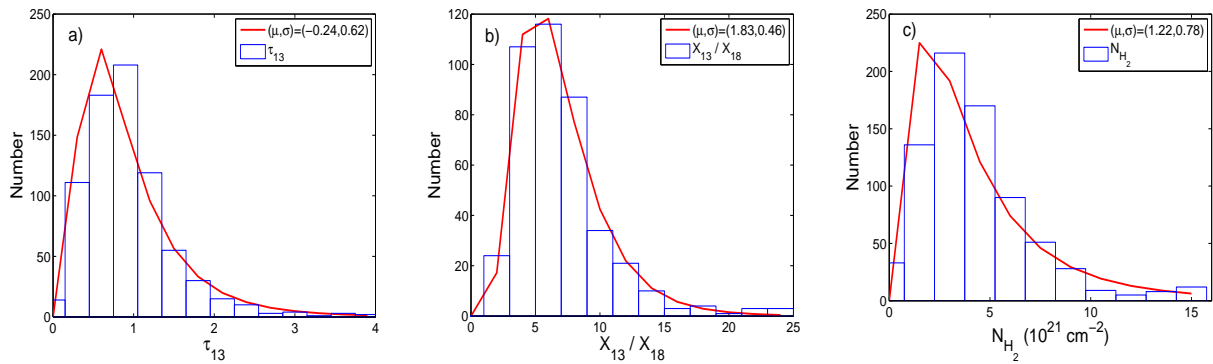


Fig. 6.— Histograms of τ_{13} , ratio $[X_{13}/X_{18}]$ and the column density N_{H_2} and their lognormal-PDF fitting

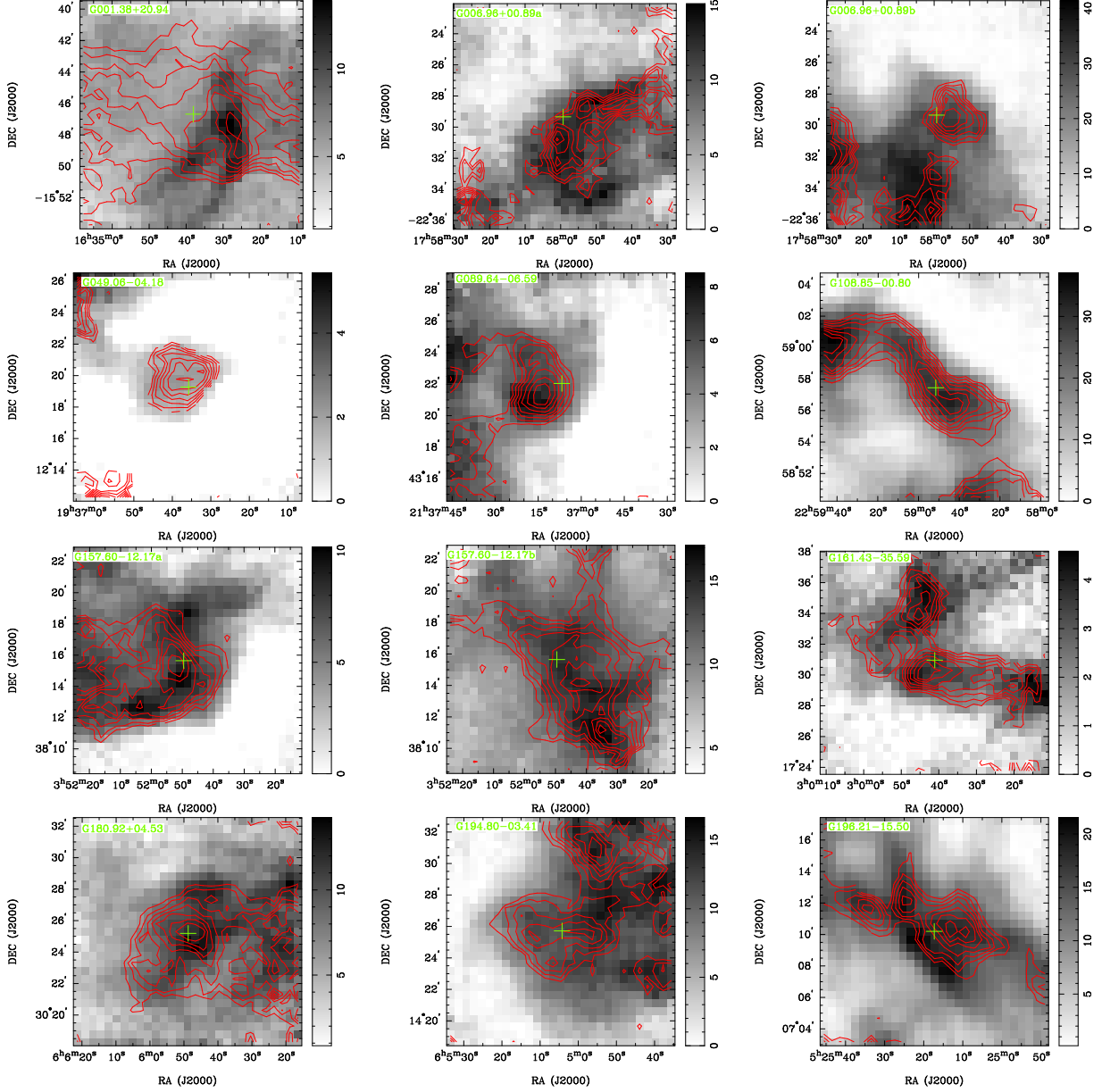


Fig. 7.— Integration intensity images of the mapped clumps: contours for ^{13}CO line and the grey scale for the ^{12}CO lines. The contours are from 30% to 90% in a step of 10% of the peak value.

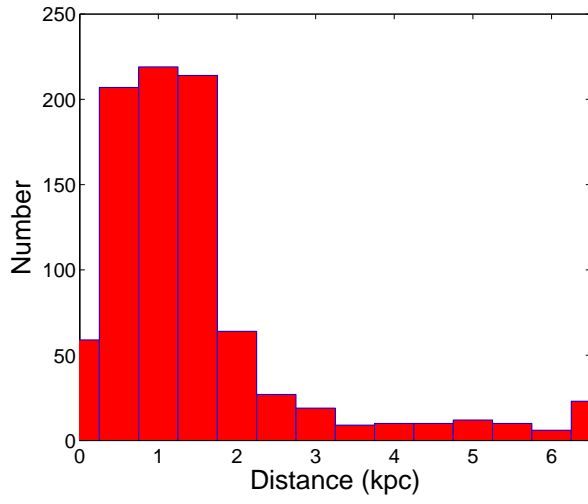


Fig. 8.— The frequency distribution of the kinematic distances

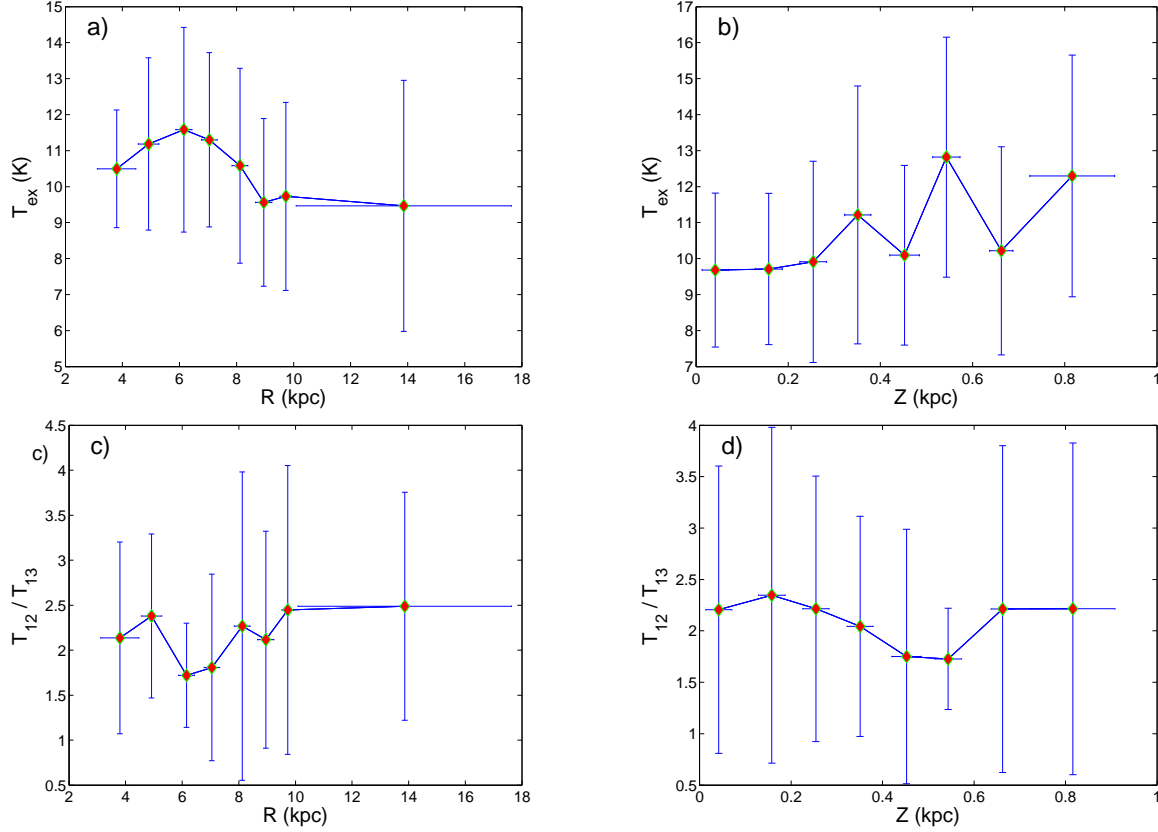


Fig. 9.— Variations of bin-averaged T_{ex} and T_{12}/T_{13} with the distance from the Galactic center R and the altitude from the Galactic disk plane Z . The bin size in R is 1 kpc for those clumps with $R < 10$ pc and the clumps with $R > 10$ pc are put into a single bin. The bin size in Z is 0.1 pc. The clumps with $Z > 1$ kpc are rare and are not included in analysis. The bin sizes in Figure 10 and 11 are the same as for figure 9.

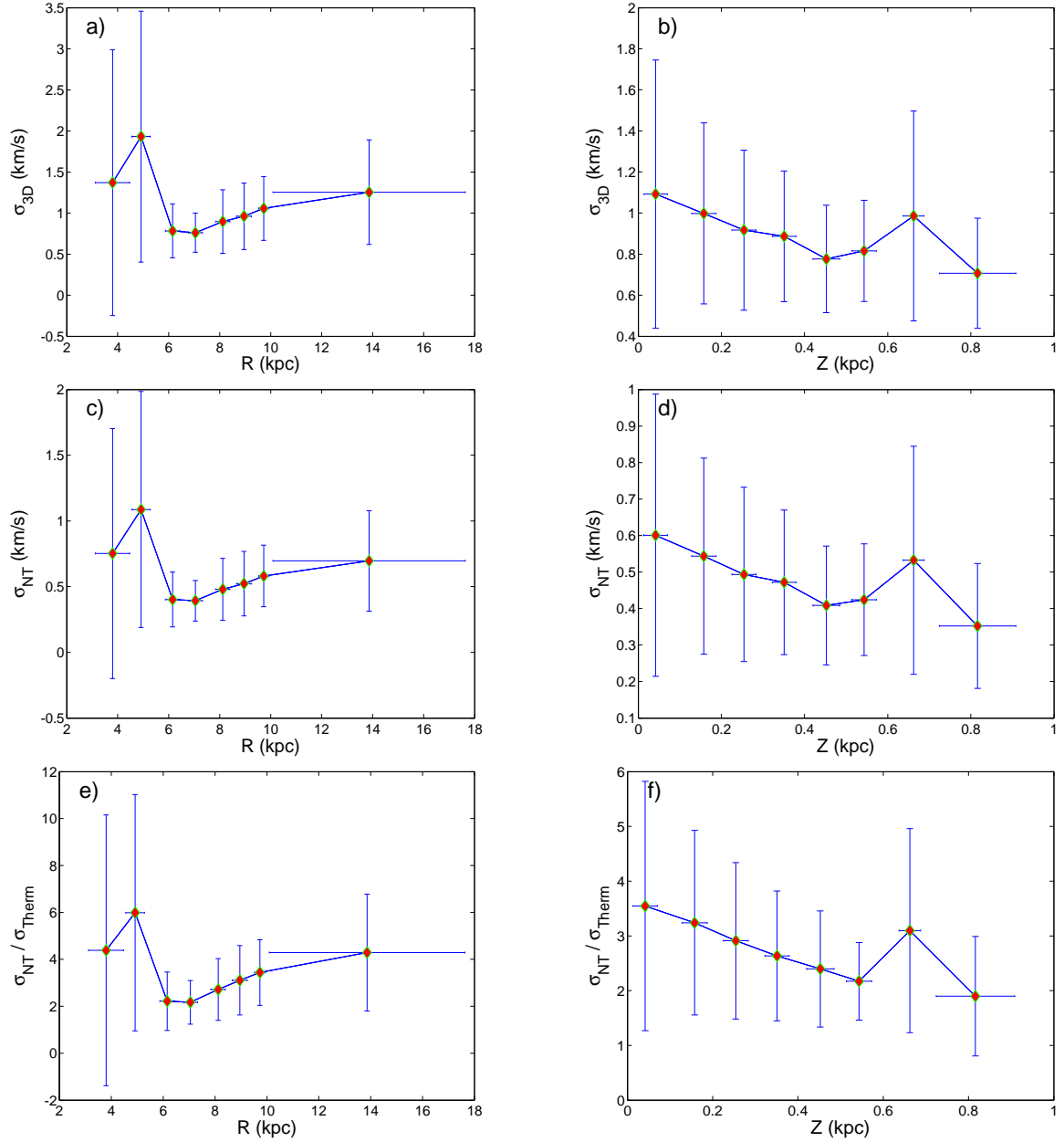


Fig. 10.— Variations of bin-averaged σ_{3D} , σ_{NT} and the ratio of $\sigma_{NT}/\sigma_{Therm}$ of ^{13}CO lines with R and Z .

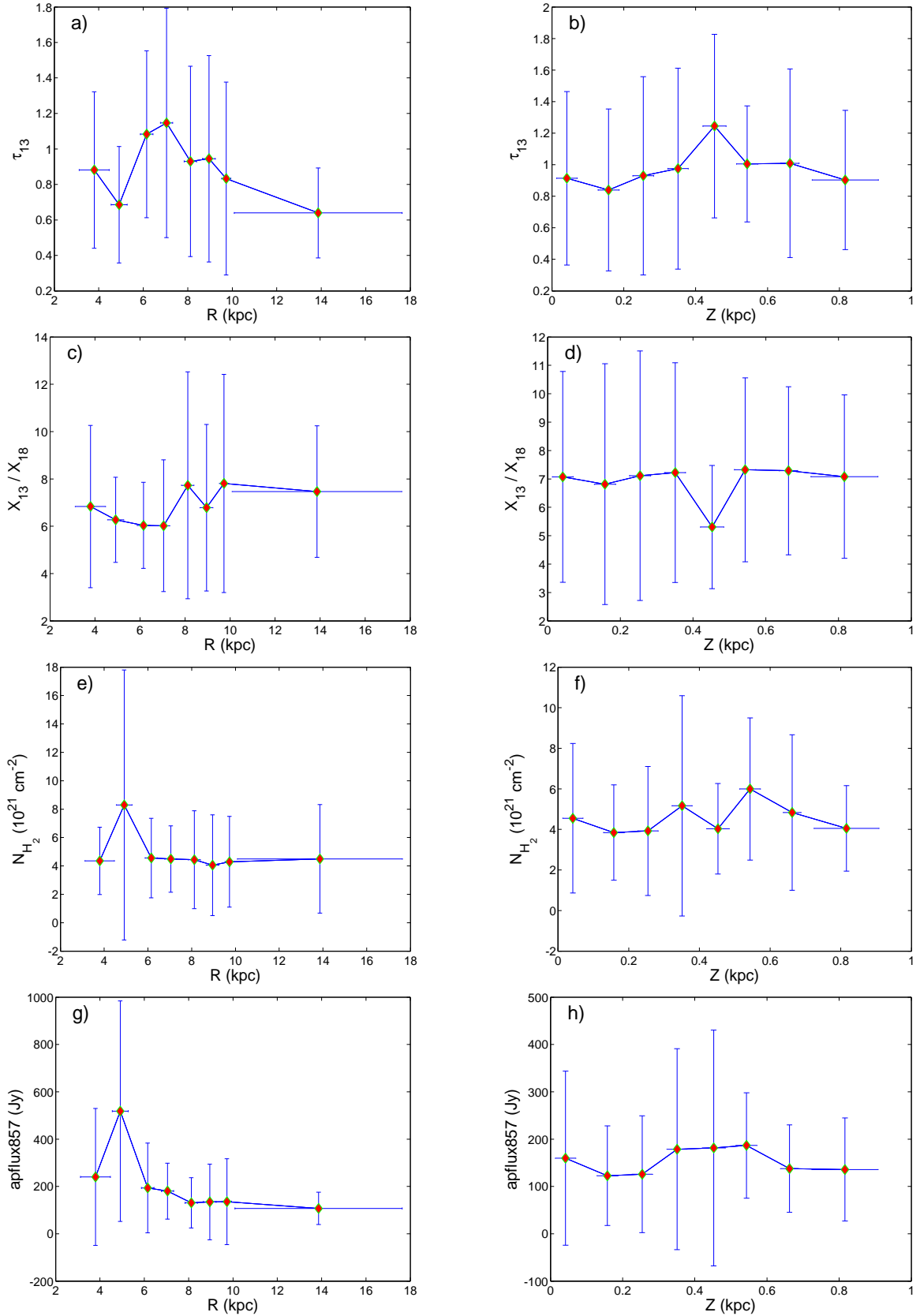


Fig. 11.— Variations of bin-averaged τ_{13} , $[X13]/[X18]$, N_{H_2} and the flux at 857 GHz with R and Z .

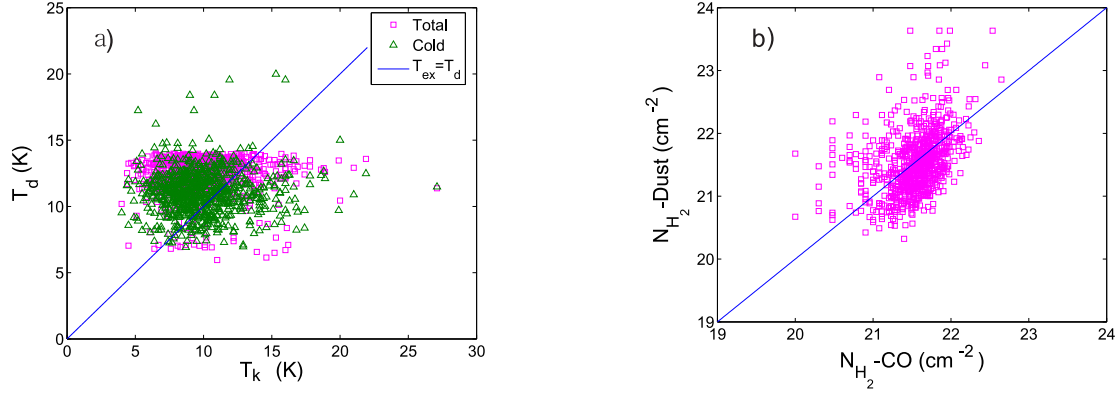


Fig. 12.— Comparison T_k to T_d and N_{H_2} to that deduced from dust emission. ”Total” and ”cold” indicate that T_d is calculated from the SED modeling with total fluxes and the SED of the residual fluxes obtained by subtracting the modeled flux from IRAS 100 μm respectively (Planck Collaboration, et al. 2011a).

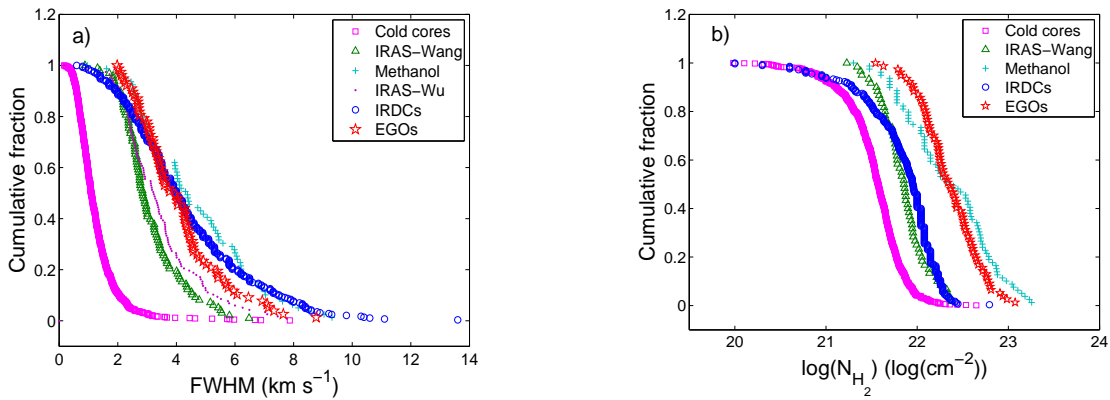


Fig. 13.— Comparisons for Cumulative fraction of FWHM of ^{13}CO lines and N_{H_2} of different star formation samples.

Table 1. Surveyed ECC clump catalogue (the first page of 22 pages)

Name	Glou (°)	Glat (°)	Ra(J2000) (h m s)	Dec(J2000) (d m s)	Ra(B1950) (h m s)	Dec(B1950) (d m s)	Region
G001.38+20.94	1.3842772	20.941952	16 34 38.06	-15 46 40.71	16 31 46.85	-15 40 30.16	Ophiuchus
G001.84+16.58	1.845703	16.587652	16 50 12.91	-18 04 22.37	16 47 18.48	-17 59 15.82	Ophiuchus
G003.73+16.39	3.7353513	16.393143	16 55 21.78	-16 43 35.31	16 52 28.86	-16 38 50.32	Ophiuchus
G003.73+18.30	3.7353513	18.308161	16 48 54.69	-15 36 02.09	16 46 03.29	-15 30 50.23	Ophiuchus
G004.02+16.64	4.0209961	16.646044	16 55 10.45	-16 21 23.27	16 52 17.98	-16 16 37.51	
G004.19+18.09	4.1967773	18.092196	16 50 42.47	-15 22 25.13	16 47 51.29	-15 17 20.75	
G004.15+35.77	4.152832	35.777241	15 53 29.82	-04 38 52.39	15 50 51.56	-04 30 01.93	High Glat
G004.17+36.67	4.1748047	36.678967	15 50 42.66	-04 04 20.84	15 48 05.00	-03 55 20.10	High Glat
G004.41+15.90	4.4165034	15.907708	16 58 35.99	-16 28 36.07	16 55 43.28	-16 24 04.69	
G004.46+16.64	4.4604487	16.646044	16 56 11.73	-16 00 51.08	16 53 19.65	-15 56 09.62	
G004.54+36.74	4.5483394	36.748764	15 51 14.27	-03 47 40.14	15 48 36.88	-03 38 41.35	High Glat
G004.81+37.02	4.8120112	37.028599	15 50 52.79	-03 27 20.38	15 48 15.74	-03 18 20.28	High Glat
G004.92+17.95	4.9218745	17.954901	16 52 50.41	-14 53 40.51	16 49 59.75	-14 48 45.05	
G005.03+19.07	5.0317378	19.076056	16 49 19.74	-14 09 20.80	16 46 30.04	-14 04 10.73	
G005.29+11.07	5.2954097	11.072874	17 17 19.97	-18 30 57.71	17 14 24.31	-18 27 45.91	
G005.29+14.47	5.2954097	14.477516	17 05 31.09	-16 36 07.96	17 02 38.08	-16 32 05.81	
G005.31+10.78	5.3173823	10.78794	17 18 23.02	-18 39 22.30	17 15 27.16	-18 36 15.00	
G005.69+36.84*	5.6909175	36.84193	15 53 11.88	-03 00 56.50	15 50 35.24	-02 52 04.98	High Glat
G005.80+19.92	5.8007808	19.926863	16 48 13.56	-13 04 14.26	16 45 25.16	-12 58 59.65	
G006.08+20.26	6.0864253	20.264484	16 47 44.35	-12 39 21.78	16 44 56.44	-12 34 05.17	
G006.04+36.74*	6.04248	36.748764	15 54 10.81	-02 50 56.32	15 51 34.33	-02 42 08.46	High Glat
G006.32+20.44	6.3281245	20.443523	16 47 40.85	-12 22 03.36	16 44 53.28	-12 16 46.52	
G006.41+20.56	6.4160151	20.562996	16 47 28.67	-12 13 52.53	16 44 41.26	-12 08 34.85	
G006.70+20.66	6.7016597	20.66263	16 47 46.71	-11 57 20.05	16 44 59.61	-11 52 03.63	
G006.96+00.89	6.965332	0.895288	17 57 59.28	-22 29 20.42	17 54 57.90	-22 29 05.02	4th Quad
G006.94+05.84	6.9433589	5.8479061	17 39 41.49	-19 58 05.07	17 36 43.62	-19 56 29.92	4th Quad
G006.98+20.72	6.9873042	20.722441	16 48 12.55	-11 42 10.17	16 45 25.73	-11 36 55.55	
G007.14+05.94	7.1411128	5.9416566	17 39 47.47	-19 45 05.14	17 36 49.87	-19 43 30.43	4th Quad
G007.53+21.10	7.5366206	21.101799	16 48 08.77	-11 03 53.56	16 45 22.69	-10 58 38.70	
G007.80+21.10	7.8002925	21.101799	16 48 43.20	-10 51 47.54	16 45 57.35	-10 46 35.08	

Table 2. Molecular complexes associated with the cold clumps.

region	l [$^{\circ}$, $^{\circ}$]	b [$^{\circ}$, $^{\circ}$]	Number	T ₁₂ (K)	T ₁₃ (K)	T ₁₈ (K)	FWHM(12) (km s ⁻¹)	FWHM(13) (km s ⁻¹)	FWHM(18) (km s ⁻¹)	N _{H₂} (10 ²¹ cm ⁻²)	T _{ex} (K)	τ(13)	X13/X18	σ _{NT} (km s ⁻¹)	σ _{Therm} (km s ⁻¹)	σ _{3D} (km s ⁻¹)
1st Quad	[12,100]	[-10,10]	84	2.69(1.20)	1.85(0.77)	0.96(0.72)	2.70(2.23)	1.73(1.34)	0.96(0.72)	5.7(5.1)	9.4(2.4)	1.1(0.9)	5.6(3.3)	0.75(0.60)	0.17(0.02)	1.34(1.02)
2nd Quad	[98,180]	[-4,10]	70	2.57(1.23)	1.67(0.77)	0.85(0.51)	2.09(1.18)	1.42(0.68)	0.85(0.51)	4.5(3.4)	9.5(2.1)	0.9(0.5)	7.6(3.3)	0.62(0.29)	0.17(0.02)	1.13(0.49)
3th Quad	[180,279]	[-4,10]	43	2.57(1.11)	1.51(0.64)	1.05(0.40)	2.90(1.00)	1.74(0.67)	1.05(0.40)	4.7(2.6)	9.1(2.0)	0.7(0.3)	7.0(2.9)	0.73(0.28)	0.17(0.02)	1.31(0.47)
4th Quad and Ctr	[300,15]	[-8,8]	6	3.09(0.44)	1.54(0.59)	2.81(5.01)	3.03(2.57)	1.83(1.96)	2.81(5.01)	4.2(2.6)	9.5(0.9)	0.8(0.4)	4.4(2.3)	0.77(0.83)	0.17(0.01)	1.39(1.42)
Anticenter	[175,210]	[-9,7]	16	2.95(0.85)	1.90(0.77)	0.80(0.44)	2.63(1.09)	1.47(0.61)	0.80(0.44)	4.7(2.1)	9.3(1.7)	0.9(0.3)	7.6(1.1)	0.67(0.24)	0.17(0.02)	1.20(0.39)
Aquila South	[27,40]	[-21,-10]	2	4.69(0.65)	2.78(0.63)	0.34(0.03)	0.83(0.16)	0.58(0.09)	0.34(0.03)	3.1(0.4)	12.8(1.3)	0.9(0.1)	9.0(0.2)	0.24(0.04)	0.20(0.01)	0.54(0.05)
Cepheus	[99,143]	[8,22]	87	2.60(0.93)	1.66(0.64)	0.69(0.29)	1.94(0.87)	1.13(0.43)	0.69(0.29)	3.5(1.9)	8.8(1.8)	1.0(0.5)	5.4(2.1)	0.48(0.18)	0.16(0.02)	0.88(0.30)
High Glat		b ≥ 25	41	3.30(1.12)	1.84(0.97)	0.46(0.18)	1.47(0.66)	0.89(0.40)	0.46(0.18)	3.0(2.0)	10.5(2.0)	0.8(0.5)	11.6(5.5)	0.37(0.17)	0.18(0.02)	0.72(0.26)
Oph-Sgr	[8,40]	[9,24]	9	3.23(1.49)	2.11(1.08)	0.42(0.16)	1.30(0.46)	0.81(0.29)	0.42(0.16)	3.0(1.6)	10.2(2.7)	0.9(0.5)	6.1(2.9)	0.34(0.13)	0.18(0.02)	0.67(0.20)
Ophiuchs	[344,4]	[7,25]	6	5.84(0.56)	3.89(0.40)	0.42(0.11)	1.10(0.23)	0.70(0.16)	0.42(0.11)	5.9(2.0)	15.0(1.2)	1.1(0.1)	7.0(5.6)	0.29(0.07)	0.21(0.01)	0.63(0.10)
Orion	[180,225]	[-25,5]	82	3.58(1.90)	2.19(1.01)	0.76(0.35)	2.12(1.02)	1.29(0.53)	0.76(0.35)	5.8(5.3)	11.1(4.0)	1.0(0.6)	8.1(5.1)	0.55(0.23)	0.18(0.03)	1.02(0.38)
Taurus	[152,180]	[-25,-3]	153	3.15(1.32)	2.08(0.86)	0.62(0.26)	1.67(0.78)	1.07(0.42)	0.62(0.26)	4.2(2.9)	10.3(2.6)	1.0(0.7)	6.2(3.4)	0.45(0.18)	0.18(0.02)	0.85(0.29)
other			75	3.45(1.61)	1.97(1.22)	0.52(0.21)	1.51(0.68)	0.92(0.45)	0.52(0.21)	3.4(2.4)	10.5(3.3)	0.9(0.7)	7.4(4.4)	0.38(0.20)	0.18(0.03)	0.75(0.31)

Table 3. Observed line parameters (the first page of 32 pages)

Name	$V_{lsr}(12)$ (km s ⁻¹)	FWHM(12) (km s ⁻¹)	$T_A(12)$ (K)	$V_{lsr}(13)$ (km s ⁻¹)	FWHM(13) (km s ⁻¹)	$T_A(13)$ (K)	$V_{lsr}(18)$ (km s ⁻¹)	FWHM(18) (km s ⁻¹)	$T_A(18)$ (K)	
G001.38+20.94	0.61(0.01)	1.16(0.02)	5.67(0.18)	0.7(0.01)	0.78(0.01)	3.98(0.09)	0.74(0.01)	0.54(0.03)	1.26(0.09)	
G001.84+16.58	6.05(0.01)	1.32(0.03)	5.58(0.17)	5.87(0.01)	0.69(0.01)	4(0.09)	5.87(0.01)	0.38(0.02)	1.67(0.09)	
G003.73+16.39	6.44(0.01)	1.11(0.02)	5.56(0.17)	6.17(0.01)	0.71(0.01)	3.41(0.09)	6.17(0.02)	0.53(0.07)	0.77(0.09)	RA
G003.73+18.30	4.44(0.01)	1.36(0.02)	6.68(0.21)	4.37(0.01)	0.97(0.01)	4.34(0.08)	4.32(0.01)	0.43(0.02)	2.45(0.08)	
G004.02+16.64	5.92(0.01)	0.69(0.02)	5.5(0.18)	5.87(0)	0.49(0.01)	3.81(0.09)	5.86(0.02)	0.34(0.05)	0.71(0.08)	
G004.19+18.09	3.64(0.01)	1.63(0.02)	5.94(0.19)	3.5(0.01)	1.23(0.01)	4.12(0.09)	3.73(0.02)	0.44(0.05)	0.94(0.08)	Dob
G004.19+18.09	6.68(0.01)	0.88(0.02)	6.63(0.19)	6.69(0.01)	0.62(0.01)	3.16(0.09)				
G004.15+35.77	2.47(0.01)	1.92(0.03)	4.72(0.14)	2.61(0.01)	1.06(0.02)	3.17(0.09)				
G004.17+36.67	2.55(0.01)	0.93(0.02)	5.08(0.17)	2.47(0.01)	0.71(0.01)	3.27(0.08)				
G004.41+15.90	4.78(0.01)	0.57(0.01)	6.11(0.15)	4.73(0)	0.48(0.01)	3.69(0.09)				
G004.46+16.64	5.16(0.01)	1.66(0.02)	6.1(0.15)	5.34(0.01)	1.19(0.02)	3.67(0.09)	5.55(0.01)	0.43(0.03)	1.42(0.09)	BA ⁺
G004.54+36.74	2.46(0.01)	1.17(0.02)	4.5(0.17)	2.53(0.01)	0.76(0.02)	2.94(0.09)	2.54(0.04)	0.44(0.1)	0.44(0.09)	
G004.81+37.02	3.6(0.01)	1.51(0.02)	4.47(0.13)	3.71(0.01)	1.04(0.02)	2.91(0.09)	3.82(0.04)	0.66(0.09)	0.46(0.08)	
G004.92+17.95	3.54(0.02)	1.49(0.03)	3.77(0.18)	3.72(0.01)	0.63(0.03)	3.26(0.17)	3.71(0.01)	0.32(0.03)	0.98(0.08)	
G005.03+19.07	3.83(0.01)	1.25(0.02)	7.17(0.19)	3.77(0.01)	0.99(0.01)	3.86(0.09)	3.81(0.03)	0.65(0.07)	0.73(0.09)	
G005.29+11.07	4.37(0.01)	0.92(0.01)	7.55(0.18)	4.22(0)	0.63(0.01)	4.07(0.09)	4.14(0.01)	0.34(0.04)	1.16(0.09)	
G005.29+14.47	3.76(0.01)	0.4(0.01)	5.07(0.18)	3.74(0.01)	0.3(0.02)	1.21(0.09)				
G005.31+10.78	4.53(0.01)	1.24(0.02)	6.56(0.19)	4.38(0.01)	0.88(0.01)	4.1(0.1)				
G005.69+36.84	0.56(0.03)	1.39(0.06)	3.84(0.17)	0.6(0.03)	0.96(0.07)	0.81(0.09)				Dob
G005.69+36.84	2.25(0.04)	1.62(0.08)	3.4(0.17)	2.33(0.01)	0.9(0.02)	3.01(0.09)	2.27(0.01)	0.4(0.02)	1.46(0.09)	
G005.80+19.92	3.45(0.01)	1.41(0.02)	6.11(0.18)	3.06(0.01)	0.89(0.01)	3.87(0.09)	2.96(0.02)	0.47(0.05)	0.99(0.09)	
G006.08+20.26	4.03(0.01)	1.95(0.02)	5.23(0.16)	3.96(0.01)	0.91(0.01)	4.19(0.08)	3.97(0.01)	0.56(0.03)	1.16(0.08)	BA ⁺
G006.04+36.74	2.34(0.02)	1.99(0.04)	3.61(0.17)	2.61(0.01)	0.94(0.02)	2.73(0.1)	2.53(0.01)	0.47(0.03)	1.47(0.09)	
G006.32+20.44	4.48(0.01)	1.6(0.02)	4.98(0.16)	4.32(0.01)	0.72(0.01)	4.25(0.09)	4.27(0.01)	0.38(0.02)	1.88(0.09)	
G006.41+20.56	4.54(0.01)	1.38(0.02)	5.9(0.16)	4.39(0.01)	0.95(0.01)	4.43(0.08)	4.44(0.02)	0.67(0.04)	1.37(0.09)	
G006.70+20.66	3.49(0.01)	2(0.03)	4.44(0.15)	3.76(0.01)	1.06(0.01)	3.97(0.08)	3.79(0.01)	0.66(0.04)	1.35(0.09)	
G006.96+00.89	9.78(0.05)	4.1(0.12)	2.66(0.23)	9.33(0.05)	2.17(0.15)	0.88(0.1)				Dob
G006.96+00.89	41.34(0.06)	9.42(0.15)	3.11(0.23)	41.53(0.1)	6.89(0.24)	0.77(0.1)	41.67(0.63)	13.03(2.05)	0.17(0.1)	
G006.94+05.84	5.22(0.02)	1.57(0.04)	3.26(0.19)	4.86(0.02)	0.63(0.06)	1.21(0.1)				Dob
G006.94+05.84	10.59(0.02)	2.57(0.05)	3.38(0.19)	10.08(0.02)	1.39(0.03)	2.22(0.1)	10.05(0.03)	0.83(0.07)	0.77(0.09)	

Table 4. Derived parameters of Surveyed ECC clumps (The first page of 40 pages)

Name	V_{lsr} (km s^{-1})	R (kpc)	D (kpc)	Z (kpc)	T_{ex} (K)	$\tau(13)$	N(13) (10^{15} cm^{-2})	$\tau(18)$	N(18) (10^{15} cm^{-2})	N_{H_2} (10^{21} cm^{-2})	ratio(12/13)	X13/X18 (km s^{-1})	σ_{NT} (km s^{-1})	σ_{Therm} (km s^{-1})	σ_{3D}
G001.38+20.94	0.74	7.47	1.1	0.39	14.8	1.2	7.3	0.2	1.6	6.5	2.1	4.6	0.32	0.21	0.67
G001.84+16.58	5.87	4.51	4.16	1.19	14.6	1.2	6.5	0.4	1.5	5.7	2.7	4.3	0.29	0.21	0.61
G003.73+16.39	6.17	5.87	2.75	0.78	14.6	0.9	5.7	0.1	1.0	5.0	2.5	5.9	0.29	0.21	0.63
G003.73+18.30	4.32	6.48	2.14	0.67	16.8	1.0	10.6	0.5	2.7	9.4	2.2	4.0	0.41	0.23	0.80
G004.02+16.64	5.86	6.10	2.52	0.72	14.4	1.2	4.3	0.1	0.6	3.9	2.0	7.7	0.20	0.21	0.50
G004.19+18.09	3.73	6.88	1.71	0.53	15.3	1.2	12.1	0.2	1.0	10.8	1.9	12.2	0.52	0.22	0.97
G004.19+18.09	6.69	5.92	2.73	0.85	16.7	0.6	4.9			4.4	3.0		0.25	0.23	0.59
G004.15+35.77	2.61	7.13	1.7	0.99	12.9	1.1	7.4			6.6	2.7		0.45	0.20	0.85
G004.17+36.67	2.47	7.19	1.64	0.98	13.6	1.0	5.2			4.7	2.0		0.29	0.20	0.62
G004.41+15.90	4.73	6.62	1.96	0.54	15.7	0.9	4.3			3.8	2.0		0.19	0.22	0.50
G004.46+16.64	5.55	6.37	2.23	0.64	15.6	0.9	10.6	0.3	1.5	9.4	2.3	7.1	0.50	0.22	0.95
G004.54+36.74	2.54	7.25	1.56	0.93	12.4	1.0	4.9	0.1	0.4	4.3	2.4	11.5	0.32	0.19	0.64
G004.81+37.02	3.82	6.79	2.15	1.30	12.3	1.0	6.6	0.1	0.7	5.9	2.2	9.9	0.44	0.19	0.83
G004.92+17.95	3.71	7.10	1.48	0.46	10.9	2.0	4.3	0.3	0.7	3.8	2.7	6.5	0.26	0.18	0.55
G005.03+19.07	3.81	7.08	1.5	0.49	17.8	0.8	9.9	0.1	1.2	8.8	2.3	8.0	0.41	0.23	0.82
G005.29+11.07	4.14	7.09	1.44	0.28	18.6	0.8	6.8	0.2	1.1	6.1	2.7	6.5	0.26	0.24	0.61
G005.29+14.47	3.74	7.20	1.35	0.34	13.6	0.3	0.8			0.7	5.6		0.11	0.20	0.40
G005.31+10.78	4.38	7.03	1.51	0.28	16.6	1.0	9.0			8.0	2.3		0.37	0.22	0.75
G005.69+36.84	0.6	8.33	0.21	0.13	11.1	0.2	1.6			1.4	6.9		0.40	0.18	0.77
G005.69+36.84	2.27	7.60	1.13	0.68	10.2	2.1	5.5	0.6	1.2	4.9	2.0	4.6	0.38	0.18	0.72
G005.80+19.92	2.96	7.52	1.05	0.36	15.7	1.0	8.3	0.2	1.1	7.4	2.5	7.4	0.37	0.22	0.75
G006.08+20.26	3.97	7.26	1.33	0.46	13.9	1.6	8.7	0.2	1.5	7.7	2.7	5.9	0.38	0.21	0.75

Table 5. Sources with blue- or red- line profiles

Name	V13 (km s ⁻¹)	FWHM13 (km s ⁻¹)	V18 (km s ⁻¹)	FWHM18 (km s ⁻¹)	V12_peak (km s ⁻¹)	δV_{13}^a	δV_{18}^b	T12_B/T12_R	ΔT^c	Profile	region
G004.46+16.64	5.34(0.01)	1.19(0.02)	5.55(0.01)	0.43(0.03)	4.95	-0.33	-1.40	1.42	1.88	blue profile	others
G006.08+20.26	3.96(0.01)	0.91(0.01)	3.97(0.01)	0.56(0.03)	3.25	-0.78	-1.29	1.09	0.42	blue profile	others
G089.03-41.28	-4.63(0.03)	1.93(0.06)			-5.37	-0.38	0.63	1.23	0.63	blue profile	High Glat
G097.09+10.12	-2.71(0.03)	1.09(0.05)	-2.67(0.04)	0.63(0.09)	-3.33	-0.57	-1.05	1.57	1.01	blue profile	others
G111.33+19.94	-7.21(0.01)	0.83(0.03)	-7.24(0.02)	0.58(0.05)	-8.13	-1.11	-1.53	1.21	0.5	blue profile	Cepheus
G111.77+13.78	-3.81(0.01)	0.85(0.03)	-3.68(0.05)	0.46(0.15)	-4.29	-0.56	-1.33	2.18	1.69	blue profile	Cepheus
G111.77+20.26	-8.06(0.01)	1.15(0.03)	-8.09(0.04)	0.88(0.11)	-8.62	-0.49	-0.60	1.84	1.55	blue profile	Cepheus
G111.97+20.52	-7.92(0.02)	0.9 (0.05)	-7.91(0.03)	0.48(0.08)	-8.62	-0.78	-1.48	1.69	0.86	blue profile	Cepheus
G117.11+12.42	3.87(0.01)	0.96(0.03)	3.92(0.02)	0.53(0.06)	3.32	-0.57	-1.13	1.25	0.78	blue profile	Cepheus
G126.49-01.30	-11.94(0.02)	1.9 (0.04)	-11.74(0.04)	0.91(0.09)	-13	-0.56	-1.38	1.19	0.6	blue profile	2nd Quad
G130.14+13.78	-1.53(0.02)	1.46(0.06)	-1.43(0.05)	0.69(0.14)	-2.55	-0.70	-1.62	1.11	0.23	blue profile	Cepheus
G155.45-14.59	1.97(0.02)	1.39(0.05)	2.13(0.03)	0.61(0.1)	0.83	-0.82	-2.13	2.50	1.93	blue profile	Taurus
G158.37-20.72	7.13(0.01)	2.35(0.02)	7.05(0.03)	1.4(0.08)	6.03	-0.47	-0.73	1.11	0.80	blue profile	Taurus
G164.94-08.57	-0.7(0.01)	1.71(0.03)	-0.63(0.05)	1.31(0.11)	-1.66	-0.56	-0.79	1.73	1.89	blue profile	Taurus
G181.84+00.31	3.3(0.02)	1.49(0.04)	3.49(0.05)	0.81(0.12)	2.21	-0.73	-1.58	1.29	0.74	blue profile	3th Quad
G190.17-13.78	1.14(0.01)	1.39(0.02)			0.74	-0.29		1.12	0.54	blue profile	Orion
G210.01-20.16	8.1(0.02)	1.83(0.04)	8.33(0.09)	0.68(0.22)	7.27	-0.45	-1.56	1.25	0.99	blue profile	Orion
G224.27-00.82	14.39(0.02)	3.04(0.04)	14.45(0.02)	1.61(0.05)	13.09	-0.43	-0.84	1.28	0.7	blue profile	3th Quad
G093.22-04.59	3.87(0.01)	1.51(0.03)	3.9(0.06)	1.14(0.15)	4.41	0.36	0.45	1.1	0.29	red profile	1st Quad
G101.14-15.28	-9.58(0.01)	0.98(0.03)			-9.18	0.41	0.29	0.92	0.29	red profile	others
G121.92-01.71	-14.07(0.01)	1.39(0.03)	-14.12(0.08)	1.11(0.16)	-13.46	0.44	0.59	0.87	0.5	red profile	2nd Quad
G145.81+10.97	-14.94(0.02)	1.06(0.04)			-14.31	0.59	0.29	0.90	0.29	red profile	others
G157.10-08.70	-7.48(0.02)	1.43(0.04)	-7.48(0.03)	0.9(0.08)	-6.98	0.35	-1.40	0.55	1.8	red profile	Taurus
G169.84-07.61	6.46(0.01)	0.67(0.02)	6.39(0.01)	0.31(0.03)	6.83	0.55	1.42	0.90	0.35	red profile	Taurus
G172.85+02.27	-17.22(0.02)	3.18(0.06)	-17.49(0.07)	1.47(0.17)	-15.83	0.44	1.13	0.90	0.45	red profile	2nd Quad
G182.15-17.95	9.4(0.01)	0.86(0.02)	9.35(0.03)	0.53(0.06)	10.11	0.83	-0.64	0.71	1.26	red profile	Orion
G182.54-25.34	1.06(0.05)	1.45(0.1)			1.78	0.50	0.87	0.74	0.87	red profile	High Glat
G188.04-03.71	3.12(0.03)	1.39(0.06)	3.15(0.08)	0.9(0.16)	4.03	0.65	-1.02	0.73	0.52	red profile	3th Quad
G192.28-11.33	10.19(0.01)	1.47(0.01)	10.13(0.04)	0.84(0.11)	10.81	0.42	0.81	0.75	1.61	red profile	Orion
G195.09-16.41	-0.08(0.01)	1.84(0.02)	-0.1(0.05)	1.3(0.13)	0.47	0.30	-0.47	0.89	0.77	red profile	Orion
G210.67-36.77	0.47(0.01)	0.6(0.02)	0.45(0.06)	0.24(0.09)	0.81	0.57	1.50	0.84	0.93	red profile	High Glat

Table 5—Continued

Name	V13 (km s ⁻¹)	FWHM13 (km s ⁻¹)	V18 (km s ⁻¹)	FWHM18 (km s ⁻¹)	V12_peak (km s ⁻¹)	δV_{13}^a	δV_{18}^b	T12_B/T12_R	ΔT^c	Profile	region
G216.69-13.88	8.72(0.02)	1.88(0.06)	8.81(0.07)	0.8(0.13)	9.71	0.53	1.13	0.91	0.32	red profile	Orion
G219.35-09.70	12.5(0.02)	1.65(0.04)	12.45(0.03)	0.93(0.07)	13.41	0.55	1.03	0.67	0.76	red profile	Orion

^a $\delta V_{13}=(V12_peak-V13)/FWHM13$

^b $\delta V_{18}=(V12_peak-V18)/FWHM18$

^c $\Delta T=abs(T12_b-T12_r)$

Table 6. Sources with blue- or red- line asymmetry

Name	FWHM13 (km s ⁻¹)	FWHM18 (km s ⁻¹)	V12 (km s ⁻¹)	V12 _{peak} (km s ⁻¹)	$\delta V(12)_{-13}^a$	$\delta V(12)_{-18}^b$	Profile	region
G018.39+19.39	0.52(0.01)	0.27(0.04)	-0.46(0.01)	-0.61	-0.29	-0.56	blue asymmetry	Oph-Sgr
G027.70-21.02	0.47(0.04)		4.95(0.02)	4.78	-0.36		blue asymmetry	
G108.10+13.19	1.04(0.04)	0.43(0.03)	-4.81(0.03)	-5.17	-0.35	-0.84	blue asymmetry	Cepheus
G111.66+20.20	1.34(0.03)	0.79(0.09)	-8.17(0.03)	-8.64	-0.35	-0.59	blue asymmetry	Cepheus
G143.85+11.49	1.63(0.08)		-13.78(0.06)	-14.3	-0.32		blue asymmetry	others
G147.96-08.02	0.63(0.1)		-28.39(0.04)	-28.59	-0.32		blue asymmetry	others
G156.90-08.49	1.92(0.06)	0.53(0.05)	-7.72(0.04)	-8.56	-0.44	-1.58	blue asymmetry	Taurus
G158.24-21.80	1.63(0.03)	1.13(0.13)	4.09(0.02)	3.45	-0.39	-0.57	blue asymmetry	Taurus
G158.40-21.86	1.21(0.03)	0.92(0.1)	4.54(0.01)	4.13	-0.34	-0.45	blue asymmetry	Taurus
G159.65+11.39	1.11(0.02)	0.99(0.27)	2.61(0.01)	1.9	-0.64	-0.72	blue asymmetry	others
G171.43-17.36	1.16(0.02)	0.4(0.03)	7.47(0.02)	6.99	-0.41	-1.20	blue asymmetry	Taurus
G172.92-16.74a	0.7(0.02)	0.51(0.08)	5.06(0.02)	4.9	-0.23	-0.31	blue asymmetry?	Taurus
G172.92-16.74b	0.87(0.02)	0.58(0.05)	6.96(0.02)	6.49	-0.54	-0.81	blue asymmetry	Taurus
G173.18-09.12	0.5(0.02)	0.51(0.09)	6.23(0.02)	6.03	-0.40	-0.39	blue asymmetry	Taurus
G179.14-06.27	0.52(0.02)		7.69(0.02)	7.45	-0.46		blue asymmetry	Anticenter
G182.02-00.16	1.28(0.05)	0.89(0.18)	3.91(0.02)	3.43	-0.38	-0.54	blue asymmetry	3th Quad
G190.08-13.51	1.62(0.03)		1.11(0.02)	0.64	-0.29		blue asymmetry	Orion
G196.21-15.50	2.29(0.08)		3.51(0.02)	2.88	-0.28		blue asymmetry	Orion
G227.70+11.18	0.59(0.14)		14.98(0.02)	14.78	-0.34		blue asymmetry	others
G003.73+16.39	0.71(0.01)	0.53(0.07)	6.44(0.01)	6.67	0.32	0.43	red asymmetry	Ophiuchus
G118.34+08.66	0.72(0.05)	0.41(0.14)	-2.07(0.03)	-1.79	0.39	0.68	red asymmetry	Cepheus
G118.36+21.74	0.86(0.06)		-3.88(0.04)	-3.5	0.44		red asymmetry	Cepheus
G142.25+05.43	0.97(0.03)		-10.18(0.01)	-9.85	0.34		red asymmetry	2nd Quad
G142.62+07.29	0.66(0.03)	0.36(0.11)	-11.42(0.02)	-10.97	0.68	1.25	red asymmetry	2nd Quad
G157.19-08.81	1.29(0.03)	0.74(0.06)	-7(0.02)	-6.49	0.40	0.69	red asymmetry	Taurus
G157.25-01.00	0.67(0.01)	0.36(0.02)	5.27(0.01)	5.5	0.34	0.64	red asymmetry	2nd Quad
G157.58-08.89	1.07(0.04)	0.41(0.03)	-6.07(0.03)	-5.37	0.65	1.71	red asymmetry	Taurus
G159.58-32.84	1.38(0.07)		3.79(0.02)	4.43	0.46		red asymmetry	High Glat
G174.50-19.88	0.81(0.02)	0.56(0.09)	7.7(0.01)	7.96	0.32	0.46	red asymmetry	Taurus
G175.16-16.74	1.11(0.03)	0.8(0.1)	5.7(0.03)	6.23	0.48	0.66	red asymmetry	2nd Quad
G195.00-16.95	1.1(0.02)	0.51(0.04)	-1.99(0.01)	-1.76	0.21	0.45	red asymmetry	Orion

Table 6—Continued

Name	FWHM13 (km s ⁻¹)	FWHM18 (km s ⁻¹)	V12 (km s ⁻¹)	V12_peak (km s ⁻¹)	$\delta V(12)_{.13}^a$	$\delta V(12)_{.18}^b$	Profile	region
G221.46-17.89	0.46(0.03)	0.17(0.66)	7.99(0.03)	8.12	0.28	0.76	red asymmetry	Orion

$$^a \delta V(12)_{.13} = (V12_peak - V12) / FWHM13$$

$$^b \delta V(12)_{.18} = (V12_peak - V12) / FWHM18$$

Table 7. A statistical analysis of parameters

Stat	V ₁₂ -V ₁₃ (km s ⁻¹)	V ₁₃ -V ₁₈ (km s ⁻¹)	T ₁₂ (K)	T ₁₂ / T ₁₃	T ₁₃ / T ₁₈	FWHM(12) (km s ⁻¹)	FWHM(13) (km s ⁻¹)	FWHM(18) (km s ⁻¹)	N _{H₂} (10 ²¹ cm ⁻²)	T _{ex} (K)	τ(13)	X13/X18	σ _{NT} (km s ⁻¹)	σ _{Therm} (km s ⁻¹)	σ _{3D} (km s ⁻¹)	σ _{NT} /σ _{Therm}
Statistics																
number ¹	782	437	904	782	437	904	782	437	782	782	782	437	782	782	782	782
mean	0.02	0	3.08	2.15	3.88	2.03	1.27	0.76	4.4	10.1	0.93	7.0	0.53	0.17	0.98	3.09
std	0.29	0.16	1.37	1.35	1.71	1.28	0.77	0.73	3.6	2.6	0.56	3.8	0.31	0.02	0.51	1.83
	normal distribution fit			lognormal distribution fit												
μ	0.02	0	1.02	0.65	1.26	0.56	0.10	-0.44	1.22	2.29	-0.24	1.83	-0.77	-1.76	-0.12	0.99
σ	0.29	0.16	0.48	0.43	0.45	0.55	0.51	0.53	0.78	0.24	0.62	0.46	0.51	-0.12	0.43	0.53
P	0	0	0	0	0.234	0.636	0.830	0.515	0	0.227	0	0.388	0.889	0.227	0.374	0.822

¹Only the parameters of ¹³CO components are analyzed. But we also include those ¹²CO components without ¹³CO emission in statistics of T₁₂ and FWHM(12). The 39 clumps without suitable reference positions in observations are excluded in statistics.

Table 8. Parameters of the ten mapped clumps

Name	V_{lsr} km s ⁻¹	d (kpc)	Offset (" , ")	Deconvolved Size (" × " (°))	R (pc)	T_{ex} (K)	N_{H_2} (10 ²¹ cm ⁻²)	σ_{Therm} (km s ⁻¹)	σ_{NT} (km s ⁻¹)	σ_{3D} (km s ⁻¹)	n (10 ³ cm ⁻³)	M_{LTE} (M_{\odot})	M_{vir} (M_{\odot})	M_J (M_{\odot})	Group	Region
G001.38+20.94	0.74	1.1	(-110,-41)	677×428(67.9)	1.4	14.1(0.9)	5.3(1.7)	0.21(0.01)	0.33(0.09)	0.67(0.13)	0.6	751	150	43	L	Ophiuchus
G006.96+00.89a_1	9.33	2.21	(5,-91)	187×119(-8.1)	0.8	9.9(0.4)	3.2(0.7)	0.17(0.00)	0.88(0.19)	1.56(0.32)	0.6	141	453	496	H	4th Quad
G006.96+00.89a_2	9.33	2.21	(-90,30)	149×102(-42.5)	0.7	9.7(0.5)	2.6(0.9)	0.17(0.00)	0.70(0.20)	1.25(0.34)	0.6	78	240	260		4th Quad
G006.96+00.89a_3	9.33	2.21	(-207,39)	301×64(-70.9)	0.7	9.4(0.3)	3.2(1.0)	0.17(0.00)	0.92(0.01)	1.61(0.17)	0.7	122	449	544		4th Quad
G006.96+00.89a_4	9.33	2.21	(-334,66)	268×143(89.1)	1.0	8.9(0.7)	2.7(0.7)	0.16(0.01)	1.02(0.30)	1.79(0.51)	0.4	204	783	945		4th Quad
G006.96+00.89b	41.67	5.36	(-64,-1)	203×161(38.2)	2.3	10.7(1.1)	6.8(2.6)	0.18(0.01)	1.52(0.22)	2.66(0.37)	0.5	2579	3873	2905	H	4th Quad
G049.06-04.18	9.93	0.6	(16,41)	239×194(-51.9)	0.3	8.9(1.2)	1.3(0.5)	0.16(0.01)	0.15(0.04)	0.39(0.05)	0.7	9	11	7	L	1st Quad
G089.64-06.59	12.51	0.6	(81,-20)	320×187(-0.9)	0.4	10.2(0.9)	3.4(1.5)	0.18(0.01)	0.40(0.09)	0.74(0.15)	1.5	30	45	38	L	1st Quad
G108.85-00.80	-49.51	5.4	(-20,-12)	776×213(45.1)	5.3	11.5(3.7)	7.7(5.4)	0.18(0.03)	0.89(0.28)	1.58(0.46)	0.2	14993	3096	858	H	2nd Quad
G157.60-12.17a	-7.75	1.17	(-38,-44)	432×283(16.4)	1.0	10.4(0.9)	3.6(1.2)	0.18(0.01)	0.40(0.01)	0.76(0.12)	0.6	243	133	61	L	Taurus
G157.60-12.17b_1	-2.58	0.47	(-83,-63)	535×421(41.7)	0.5	14.7(1.6)	4.1(1.5)	0.21(0.01)	0.43(0.11)	0.83(0.17)	1.2	82	87	55	L	Taurus
G157.60-12.17b_2	-2.58	0.47	(-197,-278)	301×196(52.2)	0.3	14.6(1.3)	4.1(1.4)	0.21(0.01)	0.60(0.13)	1.11(0.21)	2.4	22	79	92		Taurus
G161.43-35.59_1	-5.83	1.49	(60,212)	269×143(-12.5)	0.7	9.8(0.4)	2.3(0.5)	0.17(0.00)	0.29(0.06)	0.59(0.09)	0.5	79	57	29	L	High Glat
G161.43-35.59_2	-5.83	1.49	(-3,-49)	261×150(82)	0.7	12.0(1.2)	2.6(0.8)	0.19(0.01)	0.18(0.03)	0.46(0.04)	0.6	91	35	13		High Glat
G161.43-35.59_3	-5.83	1.49	(-166,-71)	387×168(87.6)	0.9	10.5(0.9)	2.2(0.5)	0.18(0.01)	0.20(0.03)	0.47(0.04)	0.4	128	47	17		High Glat
G161.43-35.59_4	-5.83	1.49	(-303,-86)	141×140(-21.1)	0.5	10.7(0.9)	1.9(0.6)	0.18(0.01)	0.25(0.06)	0.53(0.09)	0.6	34	33	21		High Glat
G180.92+04.53	0.98	3.62	(0,-12)	359×339(62.2)	3.1	9.1(0.6)	3.4(1.1)	0.17(0.01)	0.59(0.11)	1.07(0.19)	0.2	2191	817	303	H	3th Quad
G194.80-03.41_1	12.84	2.89	(-4,-19)	690×341(81.3)	3.4	9.8(0.5)	4.5(1.7)	0.18(0.01)	0.86(0.31)	1.52(0.52)	0.2	3573	1829	812	H	3th Quad
G194.80-03.41_2	12.84	2.89	(-132,331)	355×242(61.3)	2.1	10.3(0.9)	5.3(2.4)	0.17(0.01)	0.78(0.20)	1.28(0.34)	0.4	1536	784	436		3th Quad
G196.21-15.50_1	3.76	0.8	(-79,5)	276×203(54.2)	0.5	14.5(0.8)	3.1(0.9)	0.21(0.01)	0.32(0.12)	0.68(0.16)	1.1	45	49	30	H	Orion
G196.21-15.50_2	3.76	0.8	(104,126)	228×84(3.5)	0.3	15.1(0.8)	2.8(0.7)	0.21(0.01)	0.31(0.07)	0.65(0.11)	1.7	14	26	22		Orion
G196.21-15.50_3	3.76	0.8	(265,85)	256×89(60.8)	0.3	14.6(0.6)	2.5(0.9)	0.21(0.00)	0.30(0.12)	0.66(0.15)	1.4	15	30	23		Orion

